UNDERWATER ULTRASOUND

We are all familiar with sound effects such as the delay in the echo from a far-off canyon wall, the continually changing pitch in the sound of a passing train, or the distinct sound of an empty room versus one filled with furniture. Such sounds carry information about the environment, objects within it, and sources of the sound. In the underwater environment, sound, which is energy in the form of a pressure wave, replaces light and other forms of electromagnetic wave energy (such as microwaves or radar) as the paramount means to gather information. Acoustic waves experience relatively low absorption in water, with the underwater environment being relatively transparent to sound energy. Electromagnetic waves, on the other hand, are strongly absorbed by water, and thus the underwater environment is relatively opaque to electromagnetic wave energy.

The term *ultrasound* is commonly used to indicate sound at frequencies above 20,000 cycles/s (20,000 Hz). This is about five times the pitch made by the highest key on a piano, and it is above the normal range of human hearing. In this article we also use ultrasound to imply higher-frequency underwater sound, but we are less interested in hearing and more interested in how the sound frequency defines the way sound is utilized in the underwater environment. Thus we shall define *underwater ultrasound* somewhat more broadly, considering frequencies of order 10 kHz up to about 10^4 kHz as our three-decade frequency band of interest. (Note that 1 kHz = 10^3 Hz, and 1 MHz = 10^6 Hz.) The nominal upper frequency limit is again chosen from the applications point of view. There are few uses of underwater sound that use frequencies greater than about 10^4 kHz, or 10 MHz, because underwater sound at such high frequencies will, like electromagnetic energy, be quickly absorbed over a very short distance. Sound absorption remains, however, an important controlling factor for our frequency band as well. For example, when the frequency is 10 kHz, sound travels in seawater about 10 km before losing too much of its energy owing to absorption; and when the frequency is 1 MHz, this distance reduces to about 30 m.

For our purposes we will assume that sound pressure waves are harmonic waves; and sound frequency f, wavelength λ, and wave or phase speed c are related by the equation $\lambda f = c$. Also, one can define a wavenumber k and angular frequency ω with

$$\omega = 2\pi f = kc \tag{1}$$

In seawater, c is nominally 1500 m/s (but c may vary considerably with depth as discussed later), and the frequency range 10 kHz to 10^4 kHz translates to underwater sound wavelengths of order 10 to 10^{-3} cm.

Both sound wavelength and the distance over which sound travels specify the manner in which sound is used in the underwater environment. Just a few examples of the diverse applications of underwater ultrasound include: remote sensing of plankton, fish populations, and other oceanographic properties (1); depth sounding in shallow, coastal waters, high-resolution mapping of the seafloor, and underwater navigation (2,3); detection and monitoring of underwater pollutants (4); and underwater communication and telemetry (5). Many of these applications are covered by the familiar acronym sonar, which stands for *so*und *n*avigation *a*nd *r*anging. Looking ahead, this article's emphasis is on ultrasonic remote sensing of water column properties, but the topics introduced also pertain to the broader use of underwater ultrasound.

With this article limited to underwater ultrasound, we necessarily pass over the set of equally diverse applications that rely on lower-frequency underwater sound. For example, forward-looking sonars aboard military submarines and ships, down-looking sonars to measure ocean depths, and side-scan sonars used in large-scale bathymetric surveys use frequencies in the 1 kHz to 10 kHz band. When the frequency is less than about 1 kHz, sound can travel several hundred kilometers before losing its energy to the surrounding environment. At still lower frequencies (~100 Hz) the ocean becomes nearly transparent to sound. Experiments in ocean acoustic tomography (6) are conducted in this frequency band, wherein precise measurements of the travel time for sound travel over thousands of kilometers of ocean are used to infer the mean properties of the intervening ocean, such as the average temperature of the ocean. Low-frequency sound also penetrates deep into the seabed, and experiments using low-frequency sound are designed specifically to measure properties of the seabed (7). We note that Refs. 1, 3, and 7–10 discuss at length both the physics and applications of lower-frequency underwater sound and also include material germane to this article.

In the sections ahead we discuss underwater ultrasound in relation to the following topics: sound waves in fluids; the decibel scale; underwater ultrasonic transducers, calibration techniques and cavitation; propagation in heterogeneous media; absorption; reflection from boundaries; scattering from bubbles, zooplankton, and turbulent microstructure; and underwater imaging.

SOUND WAVES IN FLUIDS

Sound waves in fluid are longitudinal (compressional) waves, meaning that in the presence of a sound wave a parcel of fluid moves back and forth with a particle velocity, $\boldsymbol{u}$, that is aligned with the direction of the propagating sound wave. The result is a region of alternating pressure, slightly higher than the ambient static pressure, p_0, when the parcels bunch up and slightly lower than p_0 when the parcels spread out. The sound pressure, p, is, in fact, the pressure difference from p_0.

Accompanying the changing pressure is also a minute change in density, $\delta\rho$, from the fluid's ambient density ρ_0.

Most of our attention in this article concerns the longitudinal sound waves that exist in fluids. However, in reflection and scattering from solid objects, there can also be transverse waves for which $\boldsymbol{u}$ is perpendicular to direction of the propagating sound wave. The relationship between the longitudinal sound speed, c_L, and transverse sound speed, c_T, is given by

$$\frac{c_L}{c_T} = \sqrt{\frac{2(1-\nu)}{1-2\nu}} \tag{2}$$

where ν is Poisson's ratio, which lies in the range 0 to 0.5 for typical elastic materials (11). For a fluid $\nu = 0.5$, for aluminum $\nu = 0.3$, and for steel $\nu = 0.23$. Since our focus in this article concerns sound in fluids, for which c_T is zero, we henceforth drop the use of a subscript, and any references to sound speed will always mean longitudinal sound speed.

The *linear theory* of sound waves (see, for example, Refs. 12–14) both simplifies the mathematics and accurately predicts many of the acoustical effects encountered in underwater ultrasound. The key assumption in linear theory concerns the relative smallness of the three primary acoustic field variables p, $\delta\rho$, and $\boldsymbol{u}$. Specifically, starting with the restriction that $\delta\rho/\rho_0 \ll 1$ leads to the linearized acoustic equation of state $p = c^2\delta\rho$, with its implication that $p \ll \rho_0 c^2$. [Note how the smallness of p is evaluated against $\rho_0 c^2$, and not the ambient pressure p_0 (12,15). We will see later that p_0 plays a critical role in determining the onset of cavitation, which is a *nonlinear* underwater acoustic effect (16).] Similarly, the restriction on $\boldsymbol{u}$ is $|u|/c \ll 1$, where the ratio $|u|/c$ is the acoustic Mach number. To see how the smallness assumption is easily satisfied, take the maximum acoustic pressure 1 m in front of a typical research sonar to be 10^4 N/m^2 (N = newton). Taking ρ_0 for seawater as 1025 kg/m^3, then $\rho_0 c^2 = 2.3 \times 10^9$ N/m^2, and $|p|/\rho_0 c^2 \sim 4 \times 10^{-6}$. Moving further away from the sonar, say by a factor of 10, further reduces this ratio by a factor of 10.

The acoustic variables p, $\delta\rho$, and $\boldsymbol{u}$ are described by functions that satisfy the acoustic wave equation plus boundary conditions (e.g., see Refs. 1, 7, 13, 14, 17, and 18). In the underwater environment, boundary conditions are imposed by the sea surface, the seabed and possibly submerged objects from which sound can be reflected. In linear theory, knowing the solution of one of the acoustic variables specifies a solution to any other, and a simple solution for p that applies to many practical problems in underwater sound is that of a spherically diverging harmonic wave

$$p(t,R) = \frac{A}{R} e^{i(kR-\omega t)} \tag{3}$$

where the quantity A/R is a complex pressure amplitude that decays as $\sim 1/R$, where R is range from the source. (We will use $e^{-i\omega t}$ to represent harmonic time dependence.) Our interest is mostly in ranges far from the source, but the case $R \to 0$ is handled by noting that an actual source has some finite size, and thus wave motion never extends into the position $R = 0$ (13). Finally, the pressure as measured by a transducer is obtained by taking the real part of Eq. (3).

For a spherical wave the acoustic particle velocity is only in the radial direction, and so we drop the vector notation, writing $u(t, R)$, which relates to p through $u(t, R) = p(t, R)/Z$. The quantity Z is the spherical wave acoustic impedance given by

$$Z = \rho_0 c\left(1 - \frac{i}{kR}\right) \tag{4}$$

Note that at ranges described by $kR \gg 1$, Z becomes closer to being purely real and equal to the quantity $\rho_0 c$, which is the *characteristic acoustic impedance.* This region is known as the acoustic *far field* (13,14,17), and here p and u are in phase with each other such that sound radiation takes place, with the "radiation load" presented by the underwater medium being $\rho_0 c$. The analogy to electric fields is evident where p corresponds to voltage, u to current, and Z to electrical impedance.

The instantaneous acoustic intensity I_i is defined by the product Re(p)Re(u), where Re denotes taking the real part, and thus in the acoustic far field I_i becomes simply pu. (Note that, as with u, acoustic intensity must also in general be considered a vector quantity. However, with spherical waves, the intensity has only a radial component, and the vector notation is often suppressed.) The more commonly used acoustic field quantity is the time-averaged intensity I, which in the far field is given by

$$I = \frac{p_{\mathrm{rms}}^2}{\rho_0 c}\frac{1}{R^2} \tag{5}$$

where p_{rms} is the rms acoustic pressure, and I equals the time-averaged power per unit area (energy flux) flowing in the direction of wave propagation. For a spherical wave in the far field the acoustic pressure decays as $\sim 1/R$, and thus intensity decays as $\sim 1/R^2$, which is known as the *inverse-square law.*

Finally, a solution for p of the form

$$p = Ae^{i(kx\cos\theta + kz\sin\theta - \omega t)} \tag{6}$$

represents a *plane wave* traveling at angle θ with respect to the x axis, and the complex constant A now assumes the dimensions of pressure (dependence in a third dimension is suppressed here for simplicity). Acoustic particle velocity and pressure are again related through Z, but Z is now real and equal to $\rho_0 c$. The plane wave approximation (9) is a very useful first step in obtaining realistic solutions to many problems involving wave phenomena. For example, at a large distance from the source, spherical wave fronts are *locally planar,* and the plane wave approximation is used with local amplitude set by the $1/R$ factor associated with the region of interest. For the plane wave in Eq. (6), a propagation *vector,* $\boldsymbol{k}$, is identified with x, z components being $k \cos\theta$ and $k \sin\theta$, respectively, pointing in the plane wave's single direction of propagation and also normal to the wave's planar wave fronts. Later, in the context of propagation in media with a gradually changing sound speed, we will see how the wave vector may change its direction, and the trajectory of these changes defines an *acoustic ray*.

THE DECIBEL SCALE

Acoustic variables will ordinarily vary over several orders of magnitude, and it is often convenient to express this huge variation through a logarithmic scale. The decibel (abbreviated as dB) scale for intensity is defined by

$$\text{Value in dB} = 10\log(I/I_{\text{ref}}) \tag{7}$$

where log is base 10, and I_{ref} is a reference intensity used to relate the decibel equivalent of I back to absolute linear intensity units. In underwater acoustics, it is standard practice to set I_{ref} equal to the intensity of a plane wave with an rms pressure of 1 micropascal (μPa), equivalent to 10^{-5} dynes/cm^2. When we take $\rho_0 c$ of seawater to be 1.5×10^5 dynes s/cm^3, this sets I_{ref} equal to 0.67×10^{-22} W/cm^2. Were I to equal I_{ref}, then its decibel value would be given formally as 0 dB re 1 μPa, shorthand for 0 dB with reference to the intensity of a plane wave with a rms pressure of 1 μPa. (We shall use "re" throughout this article to denote the reference value for decibel quantities.)

The decibel scale can be used for any acoustic variable proportional to either power or intensity. Thus, to find the decibel equivalent of acoustic pressure, one must first square the pressure or equivalently compute

$$L_{\text{p}} = 20\log(p/p_{\text{ref}}) \tag{8}$$

where L_{p} means "pressure level." (It is standard practice to use capital letters for decibel variables, and refer to them as a "level.") The reference pressure is again 1 μPa rms, and therefore p must also be rms and not, say, peak pressure. For example, using the previous example of peak pressure equal to 10^4 N/m^2 1 m from the sonar, then the equivalent rms pressure expressed in μPa is 0.707×10^{10} μPa, and thus $L_{\text{p}} = 197$ dB re 1 μPa. At a range of 10 m, the pressure amplitude is reduced by a factor of 10 compared to the amplitude at 1 m owing to spherical spreading, and L_{p} decreases to 177 dB re 1 μPa. Often the decibel is used just to relate two quantities, without regard to reference. For example, the difference between two pressures, say p_1 and p_2, is expressed through 20 log p_1/p_2, giving the difference in terms of pressure level.

UNDERWATER ULTRASONIC TRANSDUCERS

An acoustic transducer is a device that converts an electric signal, such as voltage, into a pressure signal that propagates as a sound wave. Transducers are reciprocal devices, so they also carry out the reverse task of sound-to-electric conversion. (The term hydrophone applies to a device used only for sound-to-electric conversion.) The most common conversion mechanism in underwater ultrasonic transducers is the piezoelectric effect, in which the transducer material is deformed slightly when a voltage is applied across attached electrodes. These deforming vibrations produce a time-dependent pressure field in the water, $p(t)$, which propagates as a sound wave. In a like manner, a voltage signal, $v(t)$, is produced by the transducer (or hydrophone) when it is subjected to the pressure fluctuations of a sound field, which also slightly deforms the transducer material.

Modern piezoelectric materials used in ultrasonic transducers most often consist of ceramic compositions such as barium titanate ($BaTiO_3$), lead zirconate titanate (PZT), and PVDF (19,20). A typical configuration for the piezoelectric ceramic material is a thin circular plate of thickness L, where L is between $\lambda/2$ and $\lambda/4$ (19). The transducer vibrations occur in the thickness dimension, with the natural, or resonant, frequency of the transducer (f_0) being approximately proportional to L^{-1}. The exact f_0 depends on the particular piezoelectric material, how it is encased in the transducer housing, and how the transducer is networked together with system electrical components such as the driving amplifier. The transducer operates most efficiently within a frequency band centered around f_0, and the transducer's operational bandwidth is defined by $f_2 - f_1$, where f_1 and f_2 are, respectively, the frequencies below and above f_0 at which the transducer output acoustic power has fallen to 50% of maximum. The transducer Q value is defined as $f_0/(f_2 - f_1)$, with a typical Q value being about 10. A useful approach to the design and analysis of an ultrasonic transducer is to model it as an equivalent electrical circuit, representing both the electrical and mechanical properties of the transducer. More detail on this approach is provided in Refs. 19–21.

Ultimately, the transducer converts electric power, Π_{E}, to acoustically radiated power, Π_{A}, with a degree of efficiency, ϵ (typically ϵ ranges between 0.4 and 0.8), such that $\Pi_{\text{A}} = \epsilon\Pi_{\text{E}}$. If the transducer were to radiate acoustic power uniformly in all directions, then

$$\Pi_{\text{A}} = I_0 4\pi r_0^2 \tag{9}$$

where I_0 is acoustic intensity (W/m^2) at range r_0 (m) from the transducer face. We set r_0 equal to 1 m, which is the standard reference distance in underwater acoustics. Transducers that operate in this manner are known as *omnidirectional transducers.* However, most applications of underwater ultrasound require *directional* transducers that concentrate the transmitted acoustic power into a specific direction, as into an approximate cone of solid angle Ψ. Given that the transducer is reciprocal, it will also then preferentially receive sound coming from within this same directional cone and will be largely insensitive to sound coming from other directions. This property is described by the transducer's intensity pattern function $b(\theta, \phi)$ (or beam pattern for short), which is proportional to the sound intensity transmitted into, or received from, directions described by angles θ and ϕ. For omnidirectional transducers $b(\theta, \phi) = 1$ for all θ and ϕ. For a circular piston transducer of diameter, d, the theoretical beam pattern is (3,20)

$$b(\theta) = \left|\frac{2J_1[(\pi d/\lambda)\sin\theta]}{(\pi d/\lambda)\sin\theta}\right|^2 \tag{10}$$

For such transducers, b is symmetric about a central axis normal to the transducer face, or *acoustic axis,* and thus the beam pattern is completely described by only one angle. Figure 1 shows a measured $b(\theta)$ for a circular piston transducer with a diameter of 43 mm and a center frequency of 108 kHz plotted against the theoretical $b(\theta)$ based on Eq. (10). Note that both curves are plotted in a decibel scale, since $b(\theta)$ is equal to the ratio of intensity transmitted at angle θ to the intensity transmitted along the acoustic axis, or $I(\theta)/I(0)$. In this example, good agreement between the two curves occurs only in the main-lobe region. Within the side-lobe region, deviation from ideal, theoretical behavior is quite common because behavior here is more sensitive to the precise mechanical coupling between the piezoelectric disk material and its mounting within the transducer housing. However, the main lobe is by far the most important, and transducers are often

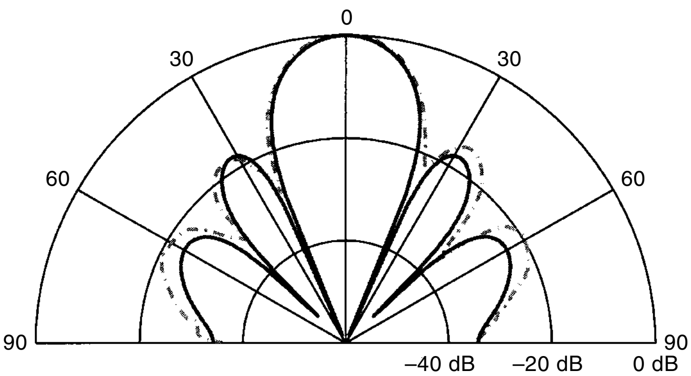

Figure 1. Measured (dashed line) and theoretical (solid line) curves representing $b(\theta)$ for a circular piston transducer with a diameter of 43 mm and a center frequency of 108 kHz.

classified by the angular width of their main lobe. A common definition is that of the beam pattern's angular width between points that are 3 dB down from the maximum on the acoustic axis. For the circular piston transducer, this width in degrees is well approximated by

$$\theta_{3\,\mathrm{dB}} \approx 60\lambda/d \tag{11}$$

The beam pattern as shown in Fig. 1 is valid only at ranges R from the transducer that are in the transducer's far field or Fraunhofer zone. For a circular piston transducer of radius a the far field is delimited by the critical range $R_c = \pi a^2/\lambda$ (9,20), which is also known as the *Rayleigh range.* Earlier we touched on the concept of the acoustic far field for a spherical wave emanating from an idealized point source. In that case the far field was defined by $kR \gg 1$, which means that range R must be large with respect to the wavelength λ. For a real transducer source, its length scale a must also be considered in defining the far-field range R. The range or a field point sufficiently distant with respect to both λ and a must satisfy $R/a \gg ka$, which is the basis of the Rayleigh range criterion. At closer ranges within the near field, or Fresnel zone, of the transducer, sound intensity varies rapidly with distance owing to the interference of the sound radiation coming from different surface elements of the transducer (1,18), and the far-field (range-independent) pattern shown in Fig. 1 is not valid.

The concentration of acoustic power into a beam is succinctly described by the *directivity factor* (3,20,22) defined as

$$\text{Directivity factor} = 4\pi / \textstyle\int b(\theta, \phi)\, d\Omega \tag{12}$$

The numerator in Eq. (12) is simply $b(\theta, \phi)$ for an omnidirectional transducer, integrated over all 4π steradians of solid angle. The denominator represents the same operation using $b(\theta, \phi)$ from a directive transducer. If we use b from a circular piston transducer of diameter d, the denominator reduces to the evaluation of

$$2\pi \int_{-\pi/2}^{\pi/2} b(\theta) \cos\theta \, d\theta \approx \frac{4\lambda^2}{\pi d^2} \tag{13}$$

and thus the directivity factor is approximately $(\pi d/\lambda)^2$. Urick (3) provides useful approximate expressions for the directivity factor of common transducer geometries. The *directivity index,* DI, is defined as 10 log of the directivity factor and is therefore equal to 10 $\log(I_d/I_{omni})$, where I_d is the intensity radiated from a directive transducer along its acoustic axis, and I_{omni} is the intensity radiated from an omnidirectional transducer with the same total acoustic power, with both measured at the same distance. A typical DI is 30 dB, meaning that the concentration of acoustic power by the directive transducer has produced 1000-fold increase in acoustic intensity.

Calibration Techniques

Transducer calibration usually means quantifying in absolute terms the transducer's ability to convert voltage to pressure (transmit voltage response) and convert pressure to voltage (receive voltage response), plus determining the transducer's beam pattern, $b(\theta, \phi)$. (There are other descriptors of transducer performance, such as input current-to-pressure response and overall transducer efficiency. Depending on the transducer application, these may or may not be determined explicitly.) It is very difficult to obtain reliable estimates of key transducer properties from theoretical calculations. The one exception is the beam pattern, where for simple transducer shapes, such as a circular piston, equations like Eq. (10) are available. But, as Fig. 1 illustrates, Eq. (10) represents an idealized beam pattern for a circular aperture, and a real transducer beam pattern will show differences particularly in the side-lobe region that are only revealed through an actual measurement.

Transducer calibration techniques fall into three basic categories; the first two are discussed at length by Bobber (23) [see also Urick (3) and Stansfield (20)], and the third is discussed by Foote (24).

1. *Comparison Method.* Properties of the unknown transducer are compared to those of a previously calibrated, or standard, transducer. The US Navy maintains several standard transducers for calibration that can be leased to other facilities. For example, the University of Washington's Applied Physics Laboratory acoustic test facility uses Navy standard transducers for calibration standards.
2. *Reciprocity Method.* The principle of reciprocity states that the transducer's receiving response in terms of pressure-to-output voltage is related to the transducer's transmitting response in terms of input current to pressure. Use of reciprocity thus allows calibration of transducers without use of a standard transducer.
3. *Calibration Sphere Method.* The echo from a solid sphere is used to calibrate the transducer. It is well known that accurate values for the echo amplitude from a sphere can be obtained through theoretical computations. For calibration purposes, the key is using a proper sphere diameter and material to avoid having strong resonant scattering effects included in the sphere's echo. For example, to calibrate 38 kHz echo sounders such as those used in fisheries research, a 60-mm-diameter copper sphere is recommended. Spheres made of tungsten carbide are also used for frequencies between 50 kHz and 500 kHz.

There is a plurality of symbolism for denoting transducer parameters. We shall use $T_x(f)$ to denote the transducer's transmit voltage response in dB re μPa per Vrms at 1 m. Whatever symbol is used, the most accepted practice is that it indicates the following: A 1 V rms sinusoidal signal of frequency f applied to the transducer leads generates a sinusoidal pressure signal at the same frequency with rms pressure of $T_x(f)$ dB re 1 μPa at a distance 1 m from the transducer face. A typical value for $T_x(f)$ at 50 kHz for a research sonar is 180 dB. Similarly, $R_x(f)$ is the receive voltage response in dB re Vrms per μPa, with a typical value for $R_x(f)$ for the same 50 kHz sonar being -120 dB.

Continuing with the above example, if the transducer is driven by a 50 kHz, 10 Vrms signal, then $L_p = 200$ dB re 1 μPa at range 1 m. As alluded to earlier, the intensity at $r_0 = 1$ m is I_0, and the transducer's *source level* (SL) is defined as 10 log I_0. Recapitulating the foregoing remarks on decibel quantities and references, if $L_p = 200$ dB, the rms pressure is 10^{10} μPa, and the SL is also 200 dB, then by definition, the intensity 1 m from the transducer is $(10^{10}\ \mu\text{Pa})^2/\rho_0 c$. This is equivalent to 67 W/m^2 or 0.67×10^{-2} W/cm^2.

Extra care must be taken to ensure consistency in the units when examining the acoustic power Π_A radiated by the transducer. Note first that an I_0 of $(1\ \mu\text{Pa})^2/\rho_0 c$ equals 0.67 10^{-18} W/m^2. If this intensity were radiated omnidirectionally, then the total radiated power would be $I_0 4\pi r_0^2$ equivalent to -171.75 dB re 1 W. Recall that for a directive transducer the power is concentrated within a beam as quantified by the directivity index DI. The total power radiated by a directive transducer given the same I_0 is $-171.75 - \text{DI}$ in dB re 1 W. We thus arrive at the very handy decibel relation between radiated power and source level:

$$\text{SL} = 10\log(\Pi_E) + 10\log(\epsilon) + \text{DI} + 171.75 \qquad (14)$$

Cavitation

Cavitation will occur if the peak amplitude of the acoustic pressure, p, approaches the hydrostatic pressure p_0. With the acoustic pressure being sinusoidal, then $p + p_0$ can take on negative values. Bubbles, or cavities, form in the evacuated negative pressure regions, causing the transducer performance to significantly degrade in terms of linearity and radiation efficiency (3,20). Erosion damage can even occur at the transducer face where bubbles preferentially form.

The onset of cavitation is determined by the *cavitation threshold* pressure. Near the sea surface, p_0 is close to 1 atm (atmosphere) or 10^{11} μPa; thus a very rough estimate of the cavitation pressure threshold, p_c, is when the peak acoustic pressure amplitude reaches 1 atm, or a pressure level of about 217 dB re 1 μPa. In fact this threshold will be somewhat higher. The cavitation threshold must increase as the operating depth increases owing to the increase in hydrostatic pressure. But there is also a time scale involved for the onset of cavitation; with increasing frequency the actual time of the negative pressure decreases, which also pushes up the cavitation threshold. Smith (25) summarizes these two effects into an empirical formula based on published data from various experiments to measure the cavitation threshold versus frequency (see also Refs. 3 and 9). The result is

$$L_c = 20\log[1 + (z/10) + (f/36)^2] + 220 \qquad (15)$$

where L_c is the cavitation threshold in dB re 1 μPa, z is depth in m, and f is frequency in kHz. As a specific example, L_c is about 229 dB re 1 μPa for a 30 kHz sonar operating within about 10 m from the sea surface, and therefore the sonar's SL should not exceed this value.

PROPAGATION IN HETEROGENEOUS MEDIA

To this point we have assumed a constant, 1500 m/s, to represent a nominal speed of sound underwater. This number is representative of the sound speed in the upper 10 m of ocean at midlatitudes; and if we remove salinity, the equivalent value in fresh water is about 1460 m/s. Nominal values for sound speed are often sufficient to handle many applications of underwater ultrasound involving short range, say on the order of 10 m. But when longer ranges are involved, it is necessary to account for the spatial and sometimes temporal variation in sound speed. The speed of sound underwater varies with temperature, salinity, and static pressure. A simplified empirical expression relating these quantities is (1)

$$\begin{aligned} c = {} & 1449.2 + 4.6T - 0.055T^2 + 0.00029T^3 \\ & + (1.34 - 0.010T)(S - 35) + 0.016z \end{aligned} \qquad (16)$$

where T is temperature (°C), S is salinity (parts per thousand), and z is depth (m). Because of space limitations we concentrate only on the effects of a depth-varying sound speed caused by temperature and salinity variation, plus the influence of increasing pressure with depth. This simplified picture is just a starting point, yet it explains many salient features of underwater sound propagation.

Ray theory (3,7,8,26) is an approximate approach for handling wave propagation in heterogeneous media, and it is particularly well-suited for underwater sound in the ultrasonic band. The validity of the ray theory hinges on the medium being slowly varying with respect to a spatial coordinate. For example, taking the variation in c with depth, a necessary but not sufficient condition (8) for the medium to be slowly varying is

$$\frac{1}{\omega}\left|\frac{dc(z)}{dz}\right| \ll 1 \qquad (17)$$

Clearly, for increasing frequency this condition becomes easier to satisfy.

To understand ray theory, we first invoke the aforementioned plane wave approximation and assume that the acoustic pressure is described by a plane wave as in Eq. (6). Let this plane wave be initially propagating in a medium with sound speed c_0 then cross into another region of water with sound speed c_1. The plane wave's propagation vector in the c_0 medium is shown by the arrow in the upper half of Fig. 2. Upon crossing the boundary separating the two media, θ_0 changes to θ_1 according to Snell's law

$$\frac{\cos\theta_0}{c_0} = \frac{\cos\theta_1}{c_1} \qquad (18)$$

which is one of the most useful expressions for the study of wave propagation. Upward refraction of the plane wave occurs if $c_1 > c_0$, downward refraction occurs if $c_1 < c_0$, and no refraction occurs if $c_1 = c_0$.

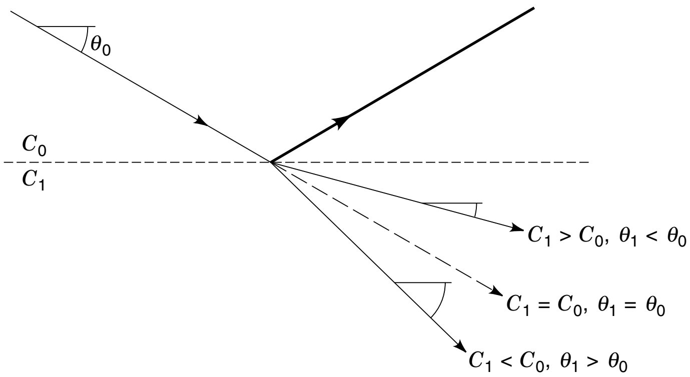

Figure 2. Example of Snell's law showing a plane wave vector in region with sound speed c_0 entering a second region with sound speed c_1.

Note that Snell's law applies exactly to the situation in Fig. 2, which also shows a ray reflected from the interface (discussed in the following section). We assume that such reflections are negligible in the following illustration of wave propagation through a medium of depth-varying sound speed, which is a very reasonable assumption provided that the sound speed undergoes gradual change in the manner of Eq. (17).

Consider next a continuously varying sound speed as a function of depth approximated by layers of differing constant speed. Snell's law in this case governs the refraction at the interface between each layer, and in the limit of vanishingly small layer thickness, Snell's law for a continuous sound speed profile $c(z)$ becomes

$$\frac{\cos\theta(z)}{c(z)} = \text{constant} \tag{19}$$

In ray theory, a ray follows the trajectory of a wave vector, whose direction may vary continuously within a medium of continuously varying sound speed. The constant in Eq. (19) is known as the *ray parameter,* a value conserved by an individual ray as it refracts within a horizontally stratified medium. It is the basis for computing ray diagrams that show the paths taken by sound as it propagates through a medium with spatially varying sound speed.

If the sound speed profile, $c(z)$, contains a local minimum, an *acoustic channel* is formed at the depth corresponding to the minimum sound speed. If a sound source were placed at or near this depth, then a ray issued from the source with negative launch angle with respect to horizontal refracts upwards, conserving its ray parameter according to Eq. (19). If the initial angle, θ_0, is sufficiently small, then $\theta(z)$ will eventually reach 0°, and the ray will begin upward travel back toward the sound speed minimum. Upon reaching the ray's starting depth, its angle is now positive θ_0, and the ray arches back toward the sound speed minimum in the same manner. The result is alternating downward and upward refraction, which traps, or channels, the ray as it cycles between the upper and lower boundaries of the channel. With sound energy now confined, it diverges cylindrically, as $\sim 1/R$, rather than spherically as $\sim 1/R^2$, allowing sound to travel to much longer ranges. The depth at which the minimum sound speed occurs is the *sound channel axis.* The most famous example of this effect is the deep sound channel, or SOFAR channel (e.g., see Refs. 3, 7, and 8). It is formed at a depth of roughly 1000 m, where the ocean's temperature approaches a constant of about 4°C. The sound speed is decreasing with increasing depth to this point, and at ~1000 m it begins increasing from the influence of hydrostatic pressure.

The SOFAR channel represents but one example of the behavior of underwater acoustic channels, or *waveguides* (7,8,26). Another consequence of refraction is the focusing and defocusing of sound energy, which can further modify either cylindrically or spherically decaying acoustic fields. To see how this occurs, consider the mean sound speed versus depth profile:

$$\begin{aligned} c(z) &= 1501, & z &\le 65\,\text{m} \\ c(z) &= 1522 - gz, & z &> 65\,\text{m} \end{aligned} \tag{20}$$

where the sound speed gradient, g, equals 0.323 s^{-1}. This equation is an approximate fit to sound speed measurements made during an experiment conducted about 400 n.mi. off the California coastline during winter conditions (27) (the equation applies only to depths less than about 200 m). The upper isospeed layer is known as a mixed layer; here turbulent mixing from winter storm activity has homogenized the temperature and salinity of the water column, producing a more uniform sound speed that we represent as a constant. Underneath the mixed layer starting at about 65 m, the thermocline leads to a steady decrease in sound speed modeled by a linear function with rate g. These two canonical sound speed regimes, isospeed and linear gradient, illustrate many of the key effects of sound refraction in the ocean.

Now consider a sound source placed at depth 150 m and a receiver at depth 50 m that is 1000 m down range. By simple application of Eqs. (19) and (20), a ray originally leaving the source with a grazing angle of 10° will have assumed a grazing angle of 5.4° when it reaches a depth of 100 m, and 0° at 80 m. At this point the ray curves downward, having reached a vertex, and will begin a steady downward travel causing it to miss the receiver completely. It is easy to show (e.g., see Refs. 1, 3, and 7) that the ray's trajectory is exactly circular while traveling within a linear gradient, with radius of curvature $R_c = c_v/g$, where c_v is the vertex sound speed of the ray, equal to 1496.28 m/s for the ray with 10° launch angle.

A collection of rays issuing from the source is shown in Fig. 3 (called a "ray trace"); these rays show the direction of energy propagation for this combination of source depth, receiver depth, range, and $c(z)$. Refraction within the linear gradient region has turned a number of rays downward, with trajectories that miss the receiver completely. Those rays with sufficiently steep launch angles eventually reach the upper isospeed layer, and continue propagating within this layer with unchanging direction until they reach the sea surface, at which point they reflect downward at the same angle. (Rays reflected from the sea surface are not shown in the figure.) We find a reduced concentration of rays that reach the vicinity of the receiver, suggesting a reduced sound intensity—that is, in excess of what we would expect based on spherical spreading alone. Finally, just below the receiver the gap between rays opens up further with no rays entering this region, known as a *shadow zone.*

The reduced sound intensity near the receiver can be quantified with more careful computations of spacing between

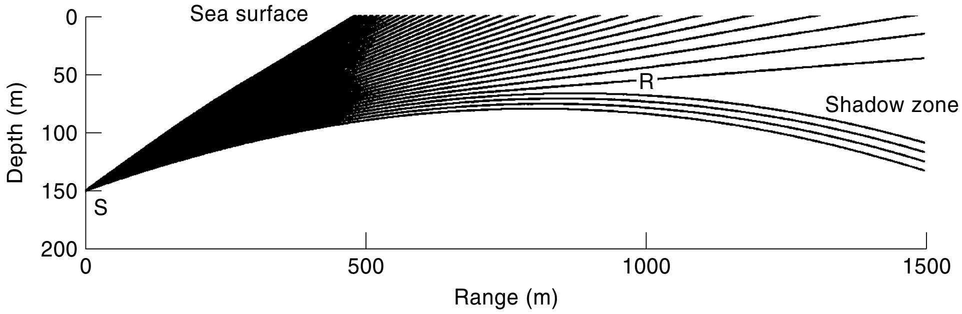

Figure 3. Ray trace corresponding to the sound speed profile of Eq. (20), with the source at 150 m and the receiver at 60 m and 1000 m down range. Rays that reach the sea surface will be reflected downward at the same angle (not shown).

rays. At the source, a pair of rays launched at $\theta_0 \pm \Delta\theta$ form a *ray tube,* which contains a fraction of the total radiated power, say $\Delta\Pi_A$. The intensity at range r_0 within the space defined by the pair of rays is I_0 and equals $\Delta\Pi_A/A_0$, where A_0 is the cross-sectional area of the ray tube. The cross-sectional area will in fact be a strip (Fig. 4) if the source were radiating omnidirectionally. Without loss of generality we proceed on this assumption and compute

$$A_0 = 2\pi r_0^2 \cos\theta_0 \Delta\theta \tag{21}$$

Energy conservation in the context of ray theory states that $\Delta\Pi_A$ must remain constant for the pair of rays over the course of their propagation path (7). The same pair of rays in the vicinity of the receiver assumes a vertical separation, Δz. At the receiver the sound speed is c_1, the local grazing angle is θ_1, and the cross-sectional area of the ray tube is

$$A_1 = 2\pi r \Delta z \cos\theta_1 \tag{22}$$

where r is the horizontal distance between source and receiver. Since A_1I_1 equals A_0I_0, the *transmission loss* (TL), defined as 10 log(I_0/I_1), is readily found to be

$$\mathrm{TL} \approx 10 \log \frac{r\Delta z \cos\theta_1}{\Delta\theta \cos\theta_0} \tag{23}$$

For the ray trace shown in Fig. 3, it is easy to take the finite-difference estimate, $\Delta z/\Delta\theta$, that approximates the true

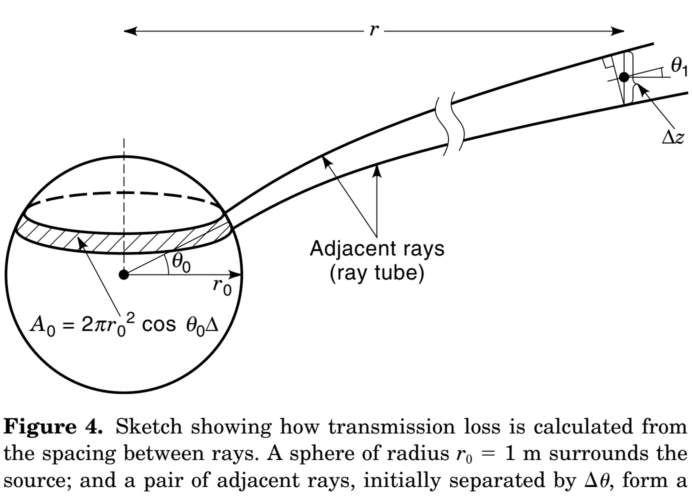

Figure 4. Sketch showing how transmission loss is calculated from the spacing between rays. A sphere of radius r_0 = 1 m surrounds the source; and a pair of adjacent rays, initially separated by $\Delta\theta$, form a ray tube that either expands or contracts depending on the sound speed of the intervening medium.

vertical rate of spreading $\partial z/\partial\theta$; and the ratio cos θ_1/cos θ_0 is, according to the now familiar Snell's law, equal to c_1/c_0. The direct path is defined by the bundle of rays that propagate directly from source-to-receiver without reflecting or scattering from the sea surface and the transmission loss for this path which is located just above the shadow zone in Fig. 3 is approximately 65 dB. If refraction effects were absent, then the transmission loss for this approximately 1000 m path would be about 20 log 1000, or 60 dB. The additional 5 dB caused by refraction is a very significant effect in terms of sonar performance.

Our simple example illustrates how ray theory can identify the key propagation characteristics associated with a particular sound speed environment and source/receiver geometry. Numerical propagation codes based on ray theory are used heavily in high-frequency sonar performance evaluations, particularly where computational speed is a critical factor. But, as mentioned previously, ray theory is an approximation, providing an ever more accurate solution to the wave equation as the frequency increases [thus ray theory is often called a high-frequency approximation (7,26)]. Two major deficiencies of ray theory are (1) *caustics,* where the area defined by a pair of rays vanishes (and thus intensity goes to infinity) and (2) *shadow zones,* where no rays can enter (and thus the intensity goes to zero). Our simple approach for computing transmission loss as outlined in Eq. (23) will fail within the shadow zone. Here, more exact solutions to the wave equation are required, and they show that the sound pressure field decays exponentially with perpendicular distance from the shadow boundary, with a decay constant proportional to $f^{1/3}$ (12).

Notwithstanding the deficiencies owing to caustics, shadow zones, and other effects, ray theory has great intuitive appeal, as illustrated by the ray trace in Fig. 3. Jensen et al. (26) outline methods to improve ray theory calculations, as well as other, more exact approaches to computing the acoustic field in inhomogeneous media based on wave theory. Frisk (7) provides a detailed discussion on the relation between solutions derived from ray theory and those derived from wave theory.

Finally, we emphasize that the ocean is neither perfectly horizontally stratified (with $\partial c/\partial r = 0$), nor frozen in time (with $\partial c/\partial t = 0$), as our Eq. (20) might suggest. Ocean salinity fronts can be crossed, and ocean dynamic processes such as tides and internal waves impart temporal variability. Apel et al. (28) provide telling examples of these effects, placed in the context of a recent shallow water acoustic propagation experiment, and Flatté et al. (29) provide a comprehensive review on this subject.

SOUND ABSORPTION

We have seen how sound intensity can decay spherically as $\sim 1/R^2$, with R being the range (in meters) from the source, and the transmission loss is given by TL = 20 log R in dB re 1 m. Transmission loss in excess of this value is possible as demonstrated in the above example. Transmission loss can also be significantly reduced if, for example, sound is confined to two-dimensional, cylindrical spreading within an acoustic channel giving TL = 10 log R. Let us collectively refer to such losses as spreading loss, and regardless of the form it takes, we must now add to it an additional loss due to *sound absorption* in water.

There are two mechanisms for absorption loss. One is a chemical relaxation in response to the passing sound wave (1). In seawater, the presence of both boric acid and magnesium sulfate is largely the cause of this absorption loss. The other is associated with viscosity and affects both seawater and freshwater (15). Absorption loss is usually expressed by α in dB/m. Francois and Garrison (30) have developed a now widely used empirical model for α shown in Fig. 5 for the 10 kHz to 10^4 kHz band. The component of α associated with boric acid is significant only for frequencies $\lesssim$10 kHz (being hardly noticeable in Fig. 5), while the component associated with magnesium sulfate dominates absorption in sea water between roughly 10 kHz and 500 kHz. Beyond about 500 kHz, viscous effects begin to dominate over chemical relaxation effects, and α increases with decreasing temperature at the same rate for both fresh- and seawater. Note that the reverse dependence occurs between about 10 kHz and 300 kHz, and α increases with increasing temperature.

The total transmission loss is the sum of spreading and absorption losses, with the latter given by αR in dB. It is important to notice that once the absorption loss approaches a significant value, it will soon dominate the total transmission loss. For example, when range R is reached such that αR = 10 dB, then a doubling of range results in another 10 dB of absorption loss, while only 6 dB additional loss is caused by spherical spreading for each doubling of range. Thus αR = 10 dB is a useful guideline to the maximum range for a given frequency; for example, at 10 kHz, $\alpha \approx 1$ dB/km, giving the 10 km mentioned at the beginning of this article as the nominal propagation range for 10 kHz.

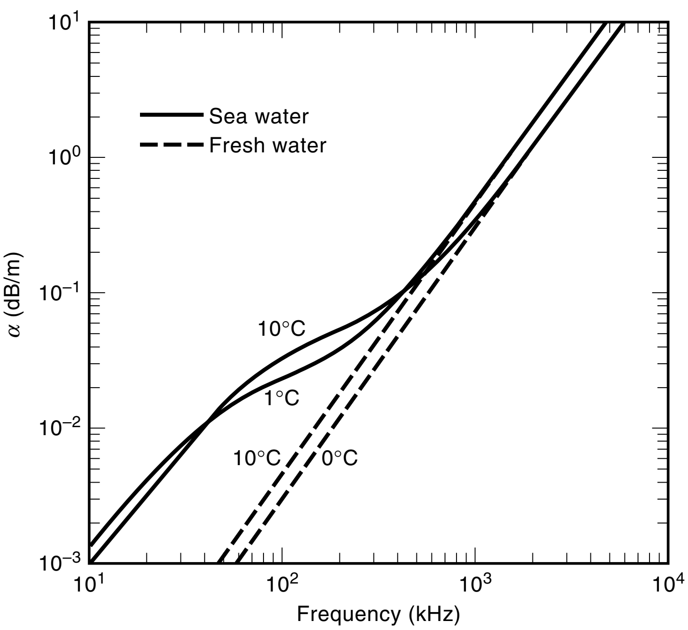

Figure 5. Attenuation rate, α (in dB/m), as computed from the François–Garrison empirical formula. Solid lines are for a water temperature of 10°C, and dashed lines are for a water temperature of 1°C. The salinity of seawater is 35 ppt.

REFLECTION FROM BOUNDARIES

Let us return to Fig. 2 and now include differing densities, ρ_0 and ρ_1, on each side of the boundary along with the differing sound speeds c_0 and c_1. Let Z_0 equal $\rho_0 c_0/\sin\theta_0$ and let Z_1 equal $\rho_1 c_1/\sin\theta_1$. These variables are *acoustic impedances,* being equal to the ratio of acoustic pressure to particle velocity in the direction normal to the boundary, evaluated at the boundary. The plane wave or Rayleigh *reflection coefficient*

$$\mathscr{R}(\theta_0) = \frac{Z_1 - Z_0}{Z_1 + Z_0} \tag{24}$$

gives the magnitude and phase of the reflected pressure wave, with the reflected wave having the same grazing angle as the incident wave. The *transmission coefficient,* $\mathscr{T} = 1 + \mathscr{R}$, gives the amplitude and phase of the pressure wave transmitted into the medium characterized by ρ_1 and c_1, with new grazing angle θ_1 (again governed by Snell's law). Reflection from the boundary between two media clearly depends on the ratio between the two characteristic acoustic impedances involved, $\rho_0 c_0$ and $\rho_1 c_1$, but also on the grazing angle as contained in Z_0 and Z_1.

The air–sea interface represents a boundary where the characteristic acoustic impedance goes from its seawater value of about 1.54×10^6 kg m^{-2} s^{-1}, or 1.54×10^6 rayls (the standard MKS unit for characteristic impedance is a *rayl* equal to 1 kg m^{-2} s^{-1}), to the substantially lesser value in air of about 430 rayls, based on a sound speed in air of 331 m/s and density of 1.29 kg/m^3. For such an extremely high contrast in characteristic impedance, it is easy to show that $\mathscr{R} \approx -1$, or $|\mathscr{R}| \approx 1$, and the phase of $\mathscr{R}$ is π. The transmission coefficient $\mathscr{T} \approx 0$, and there is a negligible amount of sound transmitted from water into the air. It is usually assumed in acoustic modeling that $\mathscr{R}$ for the air–sea interface is exactly -1.

Reflection from the seabed is considerably more varied and interesting. The ratio of seabed sediment to seawater characteristic impedance can range from nearly unity for muddy-type seabeds to $\sim$10 for extremely hard, rocky seabeds. Now let $\rho_0 c_0$ and $\rho_1 c_1$ represent seawater and seabed media, respectively. Figure 6 shows the reflection coefficient modulus $|\mathscr{R}|$ for a seabed characterized by ρ_1/ρ_0 = 1.97 and c_1/c_0 = 1.126, representing seabed sediments off Panama City, Florida (31). Absorptive losses in the seabed will also typically be quite high relative to that of seawater alone; and δ, known as the loss tangent (32,33), includes this effect by making the sound speed in the seabed complex, $c_1 \rightarrow c_1/(1 + i\delta)$. The solid line is computed with δ set to zero, and the dashed line is computed with δ = 0.0166 (31), equivalent to about 20 dB/m when the frequency is 40 kHz.

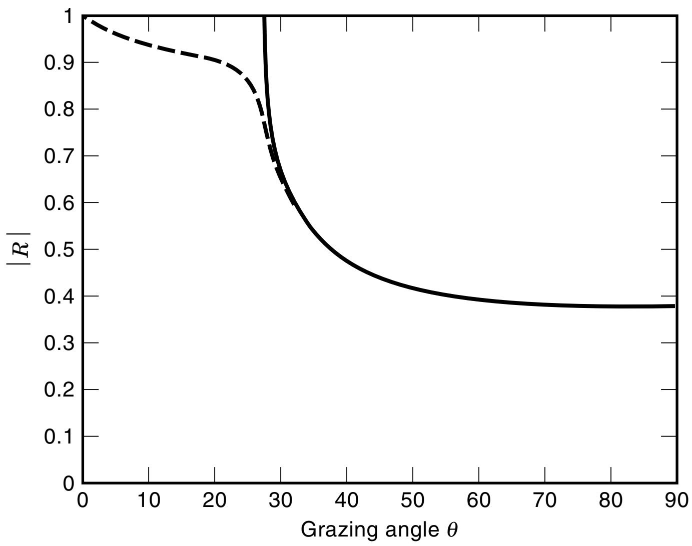

Figure 6. Magnitude of the reflection coefficient $|\mathscr{R}|$ versus grazing angle θ_0 defined relative to the horizontal. The solid line is for $\delta = 0$, and the dashed line is for $\delta = 0.0116$.

For the case of $\delta = 0$, $|\mathscr{R}| = 1$ for all grazing angles less than about 27.36°. For this range of incident grazing angles the seabed reflects all the energy back into the seawater medium (total internal reflection occurs). At exactly $\theta_c = 27.36°$, known as the *critical angle,* a transmitted wave propagates into the seabed sediment, thereby reducing the amplitude of $\mathscr{R}$. The critical angle is given by Snell's law:

$$\theta_c = \arccos(c_0/c_1) \tag{25}$$

defining the point at which θ_1 transitions from an imaginary to real angle. Energy flow into the seabed can only occur when θ_1 contains a real component; when θ_1 is purely imaginary the acoustic field in the seabed is evanescent and cannot transport energy (7). The critical angle is one of the most important acoustic parameters of the seabed; the higher the ratio of c_1/c_0, the higher the critical angle. When a nonzero δ is used, the results are modified slightly, and the complex sound speed in the seabed makes θ_1 complex for all grazing angles θ_0 (with the exception of $\theta_0 = 90°$, at which point θ_1 must also be 90° and purely real). Thus there is a small amount of energy loss into the seabed even for $\theta_0 < \theta_c$, as shown by the dashed line.

The forward reflection loss (7,32), is defined as $-20 \log |\mathscr{R}|$ and is a measure of the energy lost by sound propagating into the seabed. When $|\mathscr{R}| = 1$, the loss is 0 dB, and all the energy is trapped in the upper water layer. For the example shown in Fig. 6, the loss increases to about 8.5 dB for grazing angles greater than θ_c; and "bottom bounce" ray paths, which are common in a shallow water environment, can be substantially attenuated if their grazing angles exceed θ_c (34).

REVERBERATION AND SCATTERING PHENOMENA

Consider a plane wave incident on a small bubble having radius a with $ka \ll 1$; the bubble will *scatter* a fraction of the incident plane wave sound energy into a continuous distribution of scattering angles. We contrast this process with that of reflection from a smooth planar boundary discussed in the previous section; in that case there was only one reflected angle equal to the direction of specular reflection (not including the refracted wave that penetrates the boundary). Generally, specular reflection predominates if the object being ensonified has local radius of curvature that is large compared to the wavelength of the incident sound field (as in the case for a planar-like boundary). The term *diffraction* is sometimes used in place of scattering. Both are distinguished from reflection insofar as a distribution of scattered, or diffracted, angles is produced. But the term *diffraction* is often reserved for situations where conventional ray theory fails, such as the shadow zone example, while many problems in scattering are readily handled by ray theory methods.

Sound scattering can occur whenever sound waves traverse a region of inhomogeneities in the medium, such as a region of suspended scatterers consisting of particulate matter, biota in the form of zooplankton or fish, or bubbles. The inhomogeneities may also take the form of fluctuations in the physical properties of water such as its temperature or salinity, or fluctuations in fluid velocity associated with patches of turbulence. But for scattering to occur in this case, the fluctuations must also contain a spatial scale that is comparable to the wavelength of the incident sound field.

Volume Reverberation

Volume reverberation is the term used to describe scattering from the total volume of water ensonified. The scattering of ultrasound from entities entrained in the water provides the basis for ultrasonic remote sensing of water column properties. We thus give volume reverberation somewhat more emphasis in this article than either seafloor or sea surface reverberation, each of which pertains to the scattering contribution from the total area of ensonified sea surface or seafloor. Total reverberation is the incoherent sum of the volume and area contributions. For a source and receiver that are colocated, such as a typical transducer configuration for remote sensing applications, the reverberation is *monostatic;* and if source and receiver locations differ, the reverberation is *bistatic.*

To understand volume reverberation, we continue with the example of a small bubble with $ka \ll 1$. The bubble in fact scatters sound equally in all directions, or isotropically, and the total sound power Π_s intercepted and scattered is given by

$$\Pi_s = I_{inc}\sigma_s \tag{26}$$

where I_{inc} is the sound intensity incident on the bubble, and σ_s is the bubble's total scattering cross section in m^2 (3). Note that $\Pi_s = \int \Pi(\theta, \phi)\, d\Omega$, where $\Pi(\theta, \phi)$ is the sound power scattered toward direction $[\theta, \phi]$ away from the bubble. For isotropic scattering, $\Pi(\theta, \phi)$ is a constant, say $\Delta\Pi$, in units of power per steradian and Π_s is simply $4\pi\Delta\Pi$. For the monostatic case the quantity actually measured is the backscattered intensity from the bubble, I_{bs}, which is given by

$$I_{bs} = \frac{\Pi_s}{4\pi R^2} = \frac{I_{inc}}{R^2}\frac{\sigma_s}{4\pi} \tag{27}$$

For a bubble or any other isotropic scatterer we can thus define $\sigma_{bs} = \sigma_s/4\pi$, where σ_{bs} is the bubble's *backscattering cross section.* It is, formally, the power per unit intensity per steradian scattered in the direction toward the transducer source. For an arbitrary scatterer, such as zooplankton, which do not scatter isotropically, σ_{bs} is thus defined by its relation to I_{bs} using

$$I_{\mathrm{bs}} = \frac{I_{\mathrm{inc}}}{R^2}\,\sigma_{\mathrm{bs}} \tag{28}$$

In ultrasonic remote sensing measurements there is often need to compare relative levels of scattering, say between bubbles and zooplankton. Therefore, if the measurements represent backscattering, then it is best to both report and proceed with interpretation of σ_{bs}. If the scatterer is known to scatter isotropically, then one can report $\sigma_s = 4\pi\sigma_{bs}$ if necessary. The target strength (3), TS, is the decibel equivalent of σ_{bs}, with TS equal to 10 log σ_{bs} in dB re 1 m^2. Note that whenever target strength is evaluated, then σ_{bs} must be used and expressed in m^2.

Now consider a cloud of scatterers at range R corresponding to the cloud's center. An elemental volume dV produces a backscattered intensity at the receiver of dI_{bs}, given by

$$dI_{\mathrm{bs}} = \frac{I_{\mathrm{inc}} s_{\mathrm{V}}\, dV}{R^2} \tag{29}$$

The quantity $s_V\, dV$ assumes the role of σ_{bs} for an assemblage of scatters within a volume dV, where s_V is the backscattering cross section per unit cubic meter of water in m^{-1} (and, like σ_{bs}, must also be considered as "per steradian"). The *scattering strength,* S_V, is 10 log s_V in dB re 1 m^{-1}. Sometimes the symbol m_V is used, with the meaning of $m_V\, dV$ being total sound power scattered into all directions by volume dV. Analogous to the foregoing remarks on σ_{bs}, if it can be assumed that scattering is isotropic, then $m_V = 4\pi s_V$.

The total backscattered intensity results from summing all dV, some of which are away from the acoustic axis. For these contributions, the incident and backscattered intensity are reduced slightly according to the beam pattern $b(\theta, \phi)$. The net effect leads to the concept of an effective volume, or reverberation volume (3), based on integration of the two-way intensity pattern $b^2(\theta,\phi)$. If ψ is defined as the integral of $b^2(\theta,\phi)$ over all solid angles, then the effective volume at range R for a pulse of length τ is $(c\tau/2)R^2\psi$, and the total backscattered intensity is

$$I_{\mathrm{bs}} = \frac{I_0 r_0^2}{R^4}\, s_{\mathrm{V}} \frac{c\tau}{2} R^2 \psi \tag{30}$$

where the incident intensity is referenced back to I_0 via spherical spreading with $I_{inc} = I_0(r_0/R)^2$.)

The *sonar equation* for volume reverberation is the decibel equivalent to Eq. (30),

$$\mathrm{RL} = \mathrm{SL} - 40\log R - 2\alpha R + S_{\mathrm{V}} + 10\log\frac{c\tau}{2} R^2\psi \tag{31}$$

where the *reverberation level,* RL, is 10 log I_{bs} and the effect of two-way absorption loss is now included as $2\alpha R$. (Since $r_0 = 1$, the reference term 10 log r_0^2 is usually ignored.) Urick (3) also provides useful approximations to ψ for standard transducer shapes. Continuing with the example of circular piston transducer of diameter d, $\psi \approx 1.87(\lambda^2/\pi d^2)$, which is a factor of about 2 less than the same integral over the one-way pattern as in Eq. (13). We expect this because the equivalent two-way beam must necessarily be narrower than its one-way counterpart.

Scattering from Bubbles. Bubbles must be recognized for their particularly important role in underwater ultrasound. They are sources of scattering and attenuation (35–41), can produce changes in the sound speed (42–45), and are contributors to ambient underwater noise (46–48) (with the last set of references emphasizing noise studies in the ultrasonic band). Such effects are most evident in the vicinity of the sea surface, where bubble concentration is highest, and their numbers are continually replenished by the action of surface breaking waves. Medwin and Clay (1) summarize a portion of the more recent experimental work on ambient ocean bubble populations, which suggests that the majority of bubbles near the sea surface have radii within the range 10 μm to 1000 μm. To be sure, larger bubbles exist, but their increased buoyancy would quickly bring them to the surface. At 30 kHz, the acoustic wavenumber $k \approx 125$ m^{-1}, and thus $ka \ll 1$ over this entire range of bubble radii. In the $ka \ll 1$ regime the incident sound field is essentially uniform over the bubble's surface, and there will be a large monopole resonance response by the bubble to an incident sound field if the sound frequency matches the bubble's resonant frequency. The backscattering cross section, σ_{bs}, for a bubble in the $ka \ll 1$ regime is given by

$$\sigma_{\mathrm{bs}} = \frac{a^2}{[(f_{\mathrm{R}}/f)^2 - 1]^2 + \delta^2} \tag{32}$$

where δ is the total damping coefficient with all units in MKS (1,3). Scattering is maximal at frequency f equal to the resonant frequency f_R for a bubble radius a_R, as given approximately by

$$a_{\mathrm{R}} = \frac{3.25\sqrt{1 + 0.1z}}{f_{\mathrm{R}}} \tag{33}$$

where z is the depth.

Recall from the previous discussion that since bubbles scatter isotropically, $\sigma_s = 4\pi\sigma_{bs}$. The influence of the bubble's total scattering cross section is felt in backscattering measurements by an incremental reduction in intensity owing to the power scattered isotropically and therefore removed from the sound beam. An absorption cross section, σ_a, similarly quantifies the incremental power loss from a single bubble owing to thermal and viscous damping effects (9). Their sum $\sigma_s + \sigma_a$ gives the extinction cross section σ_e which combines the effects of absorption and scattering, with $\sigma_e = \sigma_s(\delta/ka)$.

Figure 7 shows the target stength of a bubble versus bubble radius a for bubbles near the sea surface, when they are ensonified by 30 kHz, 60 kHz, and 120 kHz. Taking 30 kHz, the maximum resonant response is produced by a bubble with a radius of 109 μm. It is interesting to compare σ_{bs} for a rigid sphere of the same radius when it is also ensonified at 30 kHz. If $ka \ll 1$, then σ_{bs} for a rigid sphere is

$$\sigma_{\mathrm{bs}} = \frac{25}{36}\, a^2 (ka)^4 \tag{34}$$

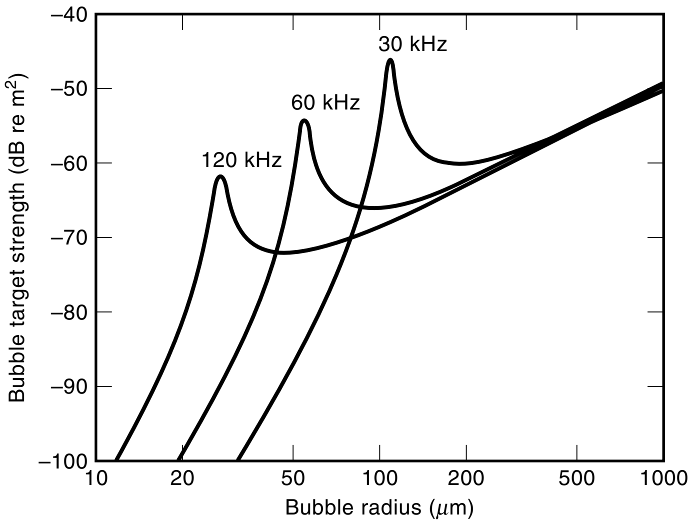

Figure 7. The target strength 10 log σ_{bs} of a bubble versus bubble radius a when ensonified by 30 kHz, 60 kHz, and 120 kHz.

and has a $(ka)^4$ dependence characteristic of Rayleigh scattering (1). For the rigid sphere, $\sigma_{bs} = 1.6 \times 10^{-16}$ compared with $\sigma_{bs} = 1.9 \times 10^{-6}$ for the same-sized bubble. Such a huge scattering advantage for bubbles when ensonified at their resonance frequency is the basis for using multifrequency acoustical backscattering techniques to remotely sense oceanic bubbles (39,41,49).

Acoustic backscattering from a cloud of bubbles is also interpreted in terms of s_V, defined in this case as the integral over bubbles of many sizes:

$$s_V = \int \sigma_{bs} N(a)\, da \tag{35}$$

where $N(a)$ is the bubble size distribution giving the number of bubbles per unit volume per unit radius, with radii between a and $a + da$. A resonant approximation (1) to this integral is

$$s_V \approx \frac{\pi a_R^3 N(a_R)}{2\delta_R} \tag{36}$$

The resonant approximation is often used for quick, initial estimates of $N(a)$, or used to obtain a starting estimate to be used in a more formal inversion procedure to obtain $N(a)$. The approximation assumes that the main portion of the integral is due to scattering from bubbles close to resonance, where δ_R is δ at resonance, which is approximated by $\delta_R \approx 0.00255 f^{1/3}$ representing a fit to measurements (50). But Eq. (36) should be used cautiously, because off-resonant contributions to the scatter can be significant; this issue is carefully addressed by Commander and Moritz (51).

For inverting and interpreting acoustic backscattering data from bubbles, an accounting must also be made for the added loss in intensity associated with propagating distance dR into the interior of a bubble cloud. The result is a bubble attenuation coefficient, α_b (in dB/m) given by (1)

$$\alpha_b = 4.34 \int \sigma_e N(a)\, da \tag{37}$$

The combined effects of scattering and absorption from bubbles can have an enormous impact on sound propagation. Recent measurements (52) made within a coastal surf zone region show that α_b can often exceed 10 dB/m at frequencies near 60 kHz (compare this with 60 kHz absorption in seawater of about 0.02 dB/m). While such high α_b are in effect, the water is essentially opaque to acoustic transmission.

Bubbles can also influence the sound speed in addition to their scattering and absorption effects. The ensuing analysis is similarly based on an integral over $N(a)$ as discussed in Ref. 1. The result is a frequency-dependent change in sound speed, $\Delta c(f) = c_0 - c_b(f)$, where c_0 and $c_b(f)$ are the speed of sound in bubble-free water and bubbly water, respectively. Lamarre and Melville (45) measured $\Delta c(f)$ near the ocean surface at wind speed of about 8 m/s. Their results show $\Delta c(f)$ to be ~20 m/s for frequencies between 10 and 20 kHz, while for higher frequencies $\Delta c(f)$ decreases, going slightly negative to about −5 m/s for their highest frequency of 40 kHz. Ultimately, $\Delta c(f)$ approaches zero as the ensonification frequency is increased well beyond the resonant frequencies associated with the population of bubbles. It is for this reason that acoustic devices for measuring the speed of sound underwater operate in the MHz frequency range and are relatively immune to the effects of bubbles on sound speed (1).

Scattering from Fish and Zooplankton. Underwater acoustic surveys in the ultrasonic band have been used to assess and manage fisheries and zooplankton stocks since the 1960s (53). In rivers of Alaska (54) and western Canada (55), sonars operating in the 100 kHz to 500 kHz range are used to count migratory salmon. Counting individual echoes from salmon is the basis for enumeration, and the sonar beams are usually oriented perpendicular to the river flow (side-scan) and approximately parallel to the river bottom (56). Trevorrow (55) discusses the issues in recognizing fish echoes from background reverberation characteristic of the riverine environment.

For more dense aggregations as found in pelagic stocks of fish and zooplankton, measurements of s_V are converted (57) to biomass in kg/m^3, or animals per m^3. For an acoustically homogeneous population of animals with density N (in number per m^3), each having the same σ_{bs}, then, according to single scattering theory (58), the observed s_V will equal $N\sigma_{bs}$. For an acoustically heterogeneous population, the relation becomes $s_V = \Sigma_i N_i \sigma_{bs_i}$. It is thus clear that accurate estimates of single fish or zooplankton target strength are essential for obtaining quantitative estimates of animal abundance. Just as with bubbles, schools of fish can also attenuate the sound. Masahiko et al. (59) measured the attenuation of sound by schooling fish at frequencies between 25 kHz and 200 kHz, for typical fish school densities encountered in field observations. Their results, however, suggest that sound attenuation by schooling fish would have a negligible effect on abundance estimates.

The sound scattering properties of a single fish at ultrasonic frequencies depend in large part on whether the fish has a swimbladder. Foote (60) demonstrated experimentally that the swimbladder contribution to σ_{bs} is approximately 90% for some combinations of fish size and acoustic frequency. For example, at 38 kHz, the target strength for a 30 cm to 35 cm length cod (swimbladdered) is about −30 dB. The target strength for a similar-sized mackerel (nonswimbladdered) is about −40 dB.

Fish orientation, or aspect, is also an important factor. For surveys of pelagic fish stocks, measurements of the *dorsal aspect* target strength are needed to quantify the data. For counting migratory salmon in rivers using side-scan sonars, the *side aspect* target strength is needed. Dahl and Mathisen (61) studied target strength variability due to aspect by rotating a fish in the yaw plane while making backscattering measurements. The side aspect target strength of a 50 cm length salmon at 420 kHz is about −25 dB, and when the fish was rotated to be head-on the target strength fell to about −45 dB, or scattering was reduced by a factor of 100.

For zooplankton, target strength depends in large part on ka_{sr}, where a_{sr}, is the animal's equivalent spherical radius equal to about 20% of its total length (57,62). For $ka_{sr} < 1$, Rayleigh scattering predominates; and therefore for a given-sized animal, σ_{bs} goes as $\sim f^4$. The optimum frequency for zooplankton studies thus clearly represents a balance between stronger scattering afforded by higher frequency and the effects of increasing absorption with frequency. Frequencies equivalent to $ka_{sr} = 0.8$ to 1.8 are suggested by Holliday and Pieper (57). Stanton et al. (63) developed a ray theory solution to the problem of sound scattering by a deformed fluid cylinder, which serves as a model for zooplankton. This work was extended (64) to handle the case of random orientation of zooplankton with respect to the sonar beam, and formulas for σ_{bs} compare favorably with measurements made over the ka_{sr} range 0.25 to 7.50.

The Doppler shift of the backscattered signal provides the component of the scatterer's velocity parallel to the sonar beam, estimated at different ranges along the sonar beam with a range resolution $\Delta R \approx c\tau/2$. If it can be assumed that the scatterers are passive tracers of the fluid velocity, then such estimates represent the actual water velocity. These scattering-based estimates of velocity are weighted by the σ_{bs} of the individual scatterers within the sonar beam (65), and on occasion they can be contaminated by the passage of stronger-scattering and actively moving fish targets. Pinkel (66) reviews Doppler sonar backscattering methods used in the study of internal wave fields, for which zooplankton are the primary source of backscatter. Plueddemann and Pinkel (67) also have used Doppler sonar to study the daily migration pattern of zooplankton within the mesopelagic zone (100 m to 1000 m). Vertical migration of a sound scattering layer (SSL) of zooplankton was observed moving toward shallower depths around sunset and toward deeper depths around sunrise, with Doppler shifts indicating a migration rate between 1 cm/s and 4 cm/s. Smith (25) discusses Doppler sonar in the context of studying near-surface dynamics, for which bubbles are the primary source of scatter and, therefore, tracers of velocity.

Scattering from Turbulent Microstructure. As alluded to at the beginning of this section, fluctuations in the physical properties of water may produce significant scattering if the spatial scale of these fluctuations is similar to the acoustic wavelength. In particular, fluctuations in the *index of refraction* $\eta(\boldsymbol{x}) = c_0/c(\boldsymbol{x})$ are related to s_V via (68,69)

$$s_V = 2\pi k^4 \Phi_\eta(\kappa_B) \tag{38}$$

where $\Phi_\eta(\kappa_B)$ is the three-dimensional wavenumber spectrum of η evaluated at its Bragg wavenumber, κ_B, which for backscattering reduces to $2k$ (70). For 100 kHz, fluctuation scales in η that are of order 1 cm are responsible for scattering; such scales are loosely classified as *microstructure*. An important issue concerns the potential ambiguities in remote sensing of zooplankton in the presence of strong turbulent fields. This was examined experimentally by Stanton et al. (71), who concluded that when zooplankton and strong turbulent fields are colocated, their separate scattering contributions can be of similar magnitude. They suggest discrimination between the two is possible through spectral analysis of echoes using broadband sonars.

Acoustic Images of Volume Reverberation

In this section we present three examples of acoustic remote sensing of water column properties, illustrating scattering from bubbles, zooplankton, and turbulent microstructure. The examples are from three separate ocean experiments, all of which used vertically oriented sonars operating in the ultrasonic band. Such measurements have the distinct advantage of being perfectly noninvasive, and they are capable of giving an unaliased picture of both biological and physical oceanographic processes.

Figure 8 is an image of S_V made with a 240 kHz uplooking sonar. The data are from an experiment conducted from the research platform *Flip,* designed to study the evolution of bubble clouds produced by breaking waves (41). The measurements were made with a sonar mounted on the end of a subsurface boom, attached to *Flip's* hull 28.5 m below the water line. With this configuration, the sonar had an unobstructed view looking up toward the surface, while *Flip* served as a very stable platform, being subjected to minimal heave motion. The wind speed is 7 m/s, and a remarkably stable bubble layer, about 3 m in thickness, is seen just below the ocean surface. An approximate mapping between the dimensionless air-void fraction β and S_V for these data is (41)

$$\log\beta \approx 0.1S_V - 4.5 \tag{39}$$

Taking $S_V = -40$ dB as representing the bubble layer puts β at about $\sim 10^{-8.5}$. The horizontal line at depth 9 m is backscatter from a lead target sphere (7 cm diameter) suspended from above by a monofilament line. Two wave crests separated by 11 s are shown on the surface (right-hand side), and the vertical displacement for the weak scattering layers (about 2 m) beneath these crests is about half the vertical displacement of the wave crests themselves, as would be predicted by linear gravity wave theory. The scattering level within these layers is about −60 dB, or 20 to 30 dB less than the scattering level from the bubbly layer, but about 20 dB greater than the expected S_V for scattering from intense turbulence (71). It is therefore postulated, as in Nash et al. (72), that these weak scattering layers are zooplankton that have congregated near horizontally stratified thermal gradients.

Figure 9 is an echogram from Mathisen and Macaulay (73) showing a dense aggregation of Antarctic krill *(Euphausia superba).* The measurements were made during the austral summer near Elephant Island in the Weddell Sea, using a 120 kHz downlooking sonar towed behind a ship at a depth of 10 m. The horizontal axis in this case represents range, and based on the ship's speed of 11 km/h the 40 min of data

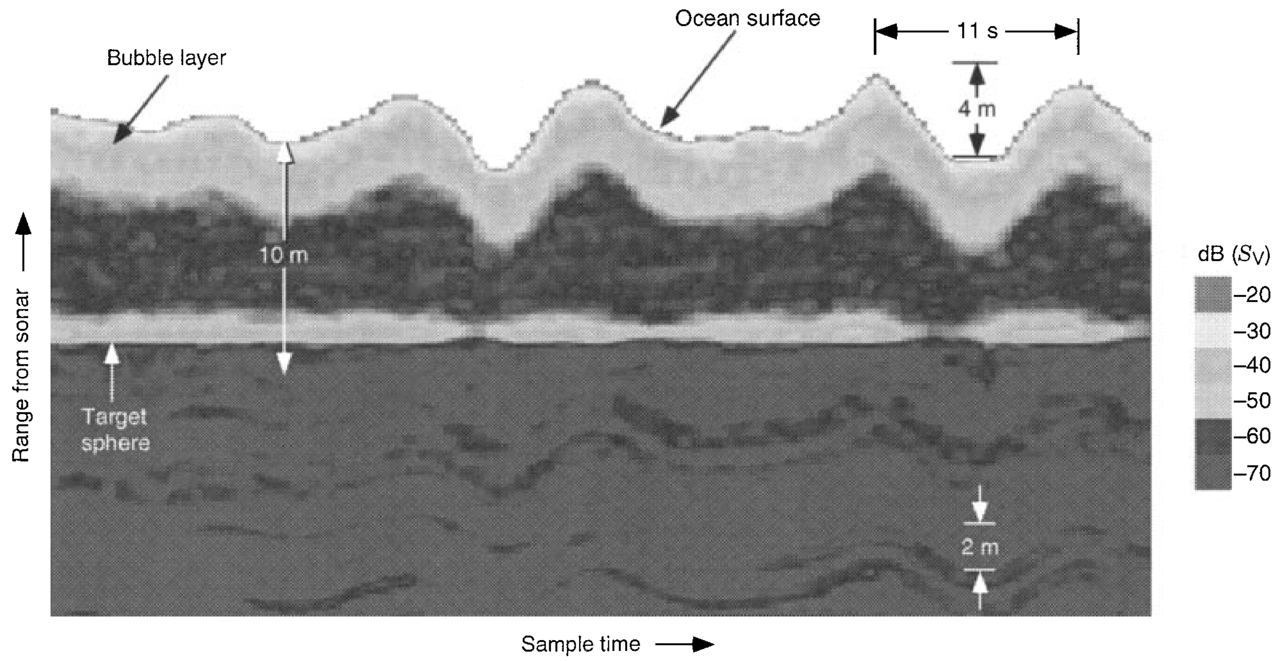

Figure 8. Acoustic volumetric backscattering from near the surface of the ocean (expressed in decibels as S_V) made with a 240 kHz uplooking sonar. Vertical axis is range from sonar, beginning at 7.5 m and extending to the ocean surface. Horizontal axis is time, with 60 s of data shown. A remarkably stable, 3-m-thick layer of bubbles is seen just beneath the ocean surface. The horizontal line at depth 9 m is backscatter from a lead target sphere (7 cm diameter) suspended from above by a monofilament line. The sphere echo fades on occasion owing to a pendulum effect. Two wave crests separated by 11 s are seen on the right-hand side, and the vertical displacement for the weak scattering layers beneath these crests is reduced by about half, as would be predicted by linear gravity wave theory.

shown here covers a 7.3 km transect. The seabed is shown on the lower left-hand side beginning at 180 m, with depth slowly decreasing over the course of the transect. The data represent a synoptic visualization of an enormous biomass of Antarctic krill. Upon remaining congregated continuously for days, as was in the case shown here, the congregation is known as super swarm.

Finally, Fig. 10 is from Pinkel et al. (74) and shows the passage of internal solitary waves (solitons) as recorded by a 167 kHz downlooking sonar in the western equatorial Pacific. The soliton wave packet consists of three downward pointing crests, the first approximately 60 m in amplitude with reduced amplitudes for the second and third crests. The backscattered intensity (proportional to S_V) increases during the passage of each crest, while decreasing slightly between crests. The authors have calculated flow streamlines (for which the tangent is parallel to the flow) shown as superscribed black lines. Upon passage of the third crest, the high scattering levels persist for approximately 4 h. The authors suggest that Bragg scattering from turbulent microstructure associated with the passage of the solitons is responsible for the enhanced scattering. The 167 kHz frequency thus implies that fluctuation scales of about 0.5 cm are responsible for the scattering.

Sea Surface and Seabed Reverberation

We return to Eq. (31), and to its left side add

$$S_S + 10 \log A \tag{40}$$

which accounts for reverberation that originates from either the sea surface or seabed. Here $S_S = 10 \log \sigma$ is the *surface* or *bottom scattering strength, A* is the sea surface or seabed area ensonified, and σ is the backscattering cross section per unit area of sea surface or seabed (3). Thus σ plays the role of σ_{bs} for area scattering, but is dimensionless, being normalized by scattering area (discussed below). Reverberation will in general have contributions from both the surface and seabed, in which case Eq. (40) is given separate treatment for each contribution.

The effective scattering area always depends on the grazing angle θ with respect to the scattering surface, the range R, and the sonar beam pattern. It may also depend on the sonar pulse length τ, in which case the area is pulse length-limited and given approximately as $A_\tau = (c\tau/2)R\Phi$, where Φ is the angle between the -3 dB points of $b(\theta)$ [given in degrees by Eq. (11)]. If the area is independent of τ, then it is beam-limited, and is given approximately as $A_b \approx (\pi/4)\Phi^2R^2/\sin(\theta)$. Careful estimates of the scattering area, however, are critical to recovering reliable estimates of S_S from field data. Jackson et al. (75) summarize an accurate approach to estimating scattering area that accounts for practical realities such as nonconical beams and seafloor slope, and Dahl et al. (76) discuss issues pertaining to beam-limiting versus pulse length-limiting estimates of the scattering area.

Volume scattering from the water column clearly affords many opportunities to invert ultrasonic measurements of S_V to gain information about the water column. With surface scattering, on the other hand, there is greater emphasis

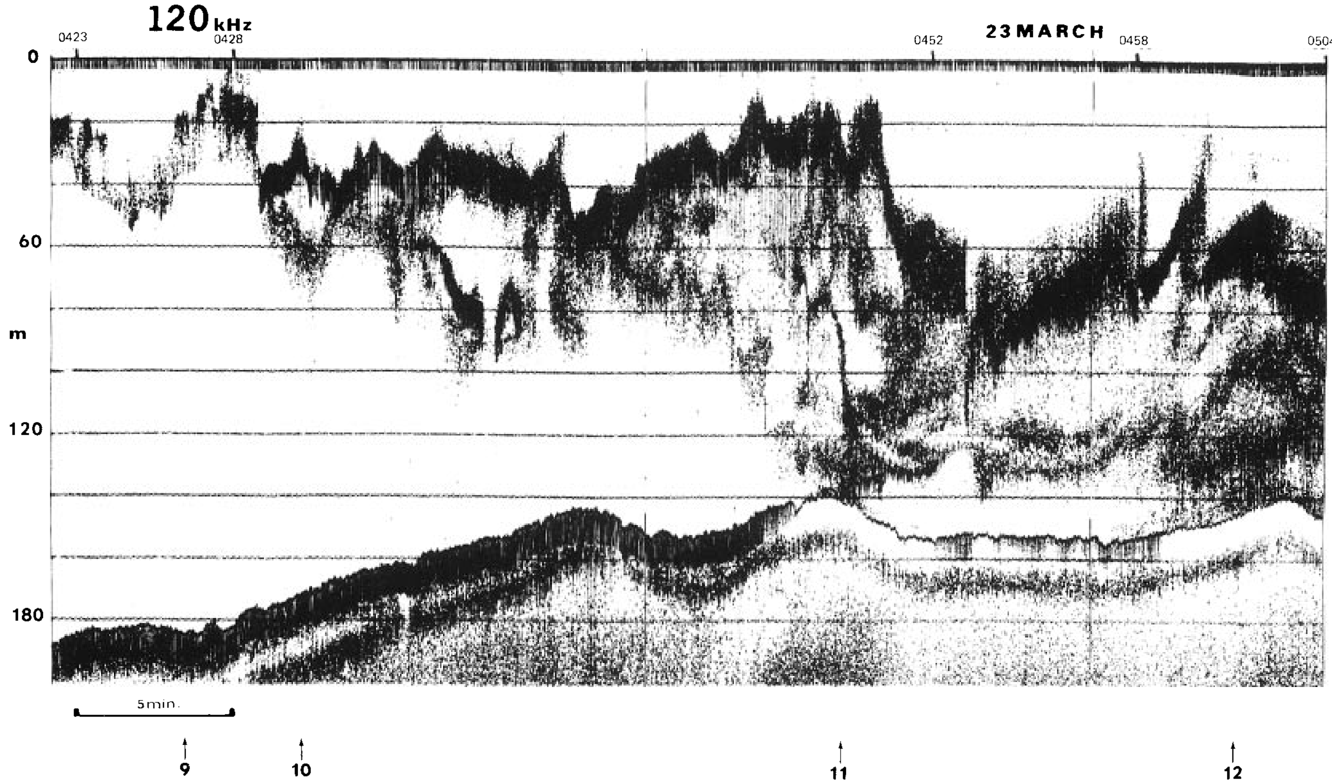

Figure 9. Echogram of super swarm of Antarctic krill, made with 120 kHz downlooking sonar on March 23, 1981 from 0423 to 0504 (GMT) near Elephant Island. The echogram pixel density is proportional to S_V. The horizontal axis is range, with total range of transect equal to 7.3 km based on total time (40 min) and speed of ship (11 km/h). The bottom is seen on the left-hand side beginning at 180 m, with depth slowly decreasing over the course of the transect. (From Ref. 73, with permission.)

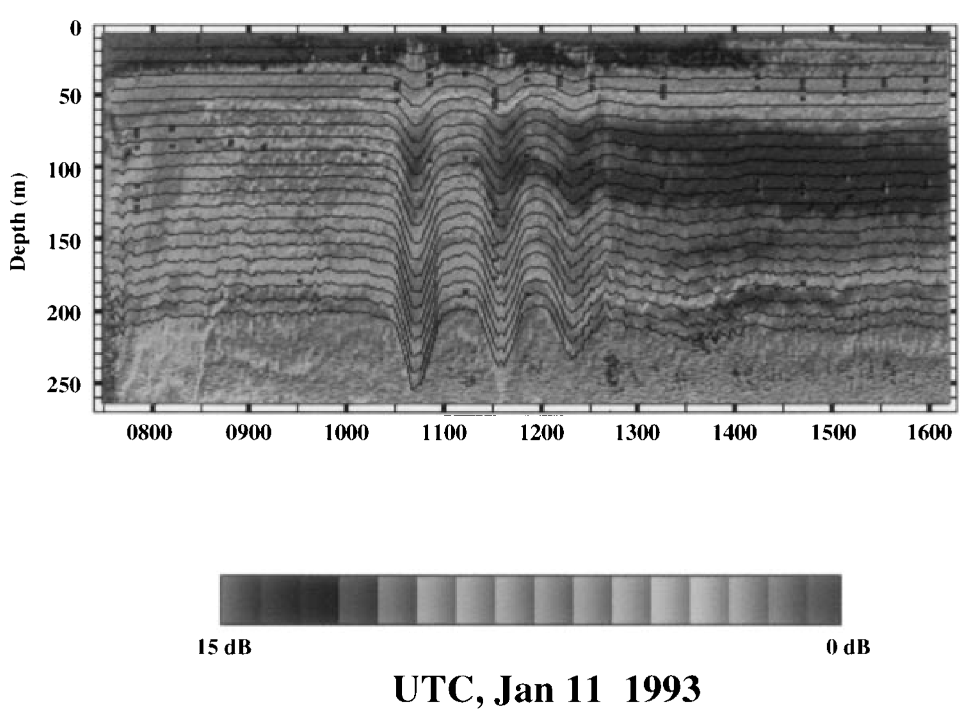

Figure 10. Acoustic scattering (proportional to S_V) as recorded by a 167 kHz downlooking sonar in the western equatorial Pacific, showing the passage of internal solitary waves. Calculated flow streamlines are shown as superscribed black lines. Black squares indicate regions of the water column with unstable density gradient. (From Ref. 74, with permission.)

placed on modeling S_S in order to determine its effect on the performance of sonar systems. McDaniel (77) provides a comprehensive review of sea surface environmental and acoustical issues that pertain to modeling sea surface reverberation. Note that within the ultrasonic frequency band, bubbles residing just beneath the sea surface are in fact the major source of sea surface reverberation (76). Variability of high-frequency acoustic backscatter from the region near the sea surface was studied by Dahl and Plant (78), who developed a model probability density function for S_S. Their study also suggested a link between acoustic variability and the passage of bubble clouds advecting through an ensonified region close to the sea surface.

Jackson et al. (31) present a model for high-frequency backscattering from the seabed and its comparison with data. The bottom reflection coefficient, as in Eq. (24), is an essential part to any model for predicting backscattering from the seabed, and the influence of the critical angle Eq. (25) is often seen in the measurements. In addition to sonar performance evaluation, physically based models for bottom scattering are now being used in the bottom classification problem, for which acoustic scattering data from the seabed are inverted to estimate seabed properties (79) or to relate temporal changes in bottom scattering to benthic changes (80).

We conclude this section with a reminder that because of space limitations and our emphasis on remote sensing applications, our treatment of reverberation has been limited to the monostatic case. There is now, however, greater interest in bistatic scattering geometries, where the source and receiver are not colocated, which has led to the development of bistatic scattering models for the seabed (33) and sea surface (81). Much of this work is motivated by the increased use of sonars on autonomous underwater vehicles operating in the ultrasonic band and used in surveillance. Time spreading (81) and angular spreading (27) also affect performance of these systems, and both are related to the sea surface or seabed bistatic scattering cross section.

ACOUSTIC IMAGING

We conclude this article on underwater ultrasound with a brief introduction to *acoustic imaging.* Figures 8 to 10 give an interesting visual display and provide valuable quantitative information on water column properties. But they are not images we commonly think of insofar as they are not both truly two-dimensional (or three-dimensional) and relatively instantaneous. (Figure 9 has true two-dimensional features, but it was gathered over a 40 min period.) However, underwater acoustic imaging systems operating at frequencies from 0.5 MHz to about 3 MHz are designed to do exactly this. For example, a three-dimensional sonar imaging system has been developed to noninvasively observe the three-dimensional swimming trajectories of zooplankton (82). Some acoustic imaging systems use acoustic lenses. Like an optical lens, an acoustic lens refracts and focuses sound to within a limited space. The real-time images provided by these systems can, for example, help divers locate and identify objects and sense the terrain in turbid waters where optical systems fail.

The primary function of an acoustic lens is to move the far field closer to the transducer, as well as provide additional focusing gain (19). The concept is exemplified by Belcher and Lynn (83), who described an experimental sonar built to inspect ship hulls for fouling and damage in turbid waters. The required resolution is 1 cm at maximum range of about 2.4 m, equivalent to an angular resolution of about 0.24°. The system's 12-cm-wide transducer operating at 3 MHz meets the requirements for angular resolution [e.g., see Eq. (11)], but the system's far field exceeds 20 m. The system's plano-concave lens, however, brings the far-field resolution back closer to the transducer and to within the specified operation range between 1.7 m and 2.4 m.

The *object plane* refers to the surface to be imaged, and the *image plane* refers to the surface upon which the image is formed (such as the retina of our eye). An example of an acoustic lens is illustrated in Fig. 11, which shows a line-focus system that maps a line in the object plane to a line on the image plane (84). In practice, the object plane is slanted with respect to the beam axis, and the acoustic imaging system thus interrogates the object plane along the line as a function of time [Fig. 11(b)].

Figure 12 shows an image taken with a line-focusing system with azimuthal resolution of 0.25°. For this demonstration, the lens was positioned 3 m above the bottom, and the system generated a single beam that was mechanically scanned across the bottom to form an image of lines from the bottom object plane every 20 s. A line-focusing system such as this has now been incorporated into a diver hand-held sonar that also operates at 750 kHz (85). In this case there are 64 beams, each ensonifying a narrow strip, and together they form a sector display that covers a 40° field of view. The image display is refreshed with new data nine times per second, or essentially in real time.

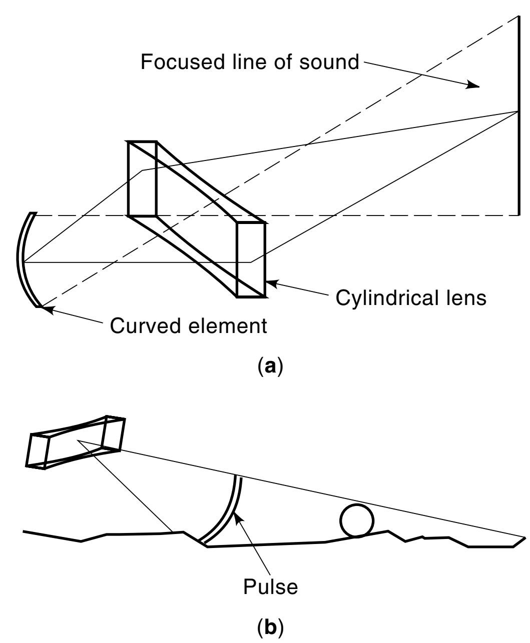

Figure 11. Illustration of a line-focus system. (a) A focused line of sound is made by the combination of cylindrical lens and curved transducer element. The lens forms the azimuthal pattern (solid lines), and the curved element forms the elevation pattern (dashed lines). (b) A pulse from a line-focus system generates a series of echoes returning from the ensonified line on the bottom. (From Ref. 84, © 1996, IEEE, with permission.)

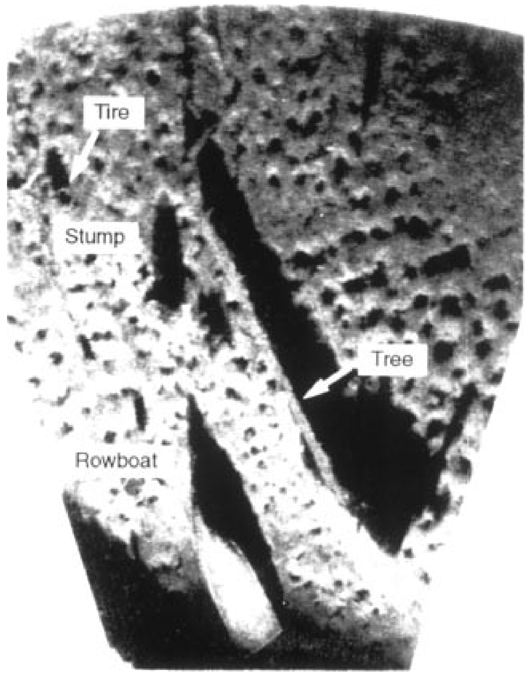

Figure 12. An image made with a line-focus system. An upside-down rowboat, an automobile tire, a tree trunk, and a stump are imaged on the pockmarked mud bottom of Lake Union in Seattle. (From Ref. 84, © 1996, IEEE, with permission.)

BIBLIOGRAPHY

1. H. Medwin and C. S. Clay, *Fundamentals of Acoustical Oceanography,* San Diego, CA: Academic Press, 1998.
2. R. C. Spindel, Oceanographic and navigational instruments, in M. C. Crocker (ed.), *Encyclopedia of Acoustics,* Vol. I, New York: Wiley, 1997, pp. 581–589.
3. R. J. Urick, *Principles of Underwater Sound,* New York: McGraw-Hill, 1983.
4. M. H. Orr and F. R. Hess, Remote acoustic monitoring of natural suspensate distributions, active suspensate resuspension, and slope/shelf intrusions, *J. Geophys. Res.,* **83**: 4062–4068, 1978.
5. J. A. Catipovic, Acoustic telemetry, in M. C. Crocker (ed.), *Encyclopedia of Acoustics,* Vol. I, New York: Wiley, 1997, pp. 591–596.
6. W. Munk, P. Worcester, and C. Wunsch, *Ocean Acoustic Tomography,* Cambridge, UK: Cambridge Univ. Press, 1995.
7. G. V. Frisk, *Ocean and Seabed Acoustics: A Theory of Wave Propagation,* Englewood Cliffs, NJ: Prentice-Hall, 1994.
8. I. Tolstoy and C. S. Clay, *Ocean Acoustics Theory and Experiment in Underwater Sound,* New York: American Institute of Physics, 1987.
9. C. S. Clay and H. Medwin, *Acoustical Oceanography: Principles and Applications,* New York: Wiley, 1977.
10. W. S. Burdic, *Underwater Acoustic System Analysis,* Englewood Cliffs, NJ: Prentice-Hall, 1984.
11. H. Kuttruff, *Ultrasonics: Fundamentals and Applications,* Amsterdam: Elsevier, 1991.
12. P. M. Morse and K. U. Ingard, Linear acoustic theory, in S. Flügge (ed.), *Handbuch der Physik,* Vol. XI/1, Berlin: Springer-Verlag, 1961.
13. P. M. Morse and K. U. Ingard, *Theoretical Acoustics,* New York: McGraw-Hill, 1968, reprinted by Princeton Univ. Press, Princeton, NJ, 1986.
14. A. P. Dowling and J. E. Ffowcs Williams, *Sound and Sources of Sound,* Chichester, UK: Ellis Horwood, 1983.
15. R. T. Beyer and S. V. Letcher, *Physical Ultrasonics,* New York: Academic Press, 1969.
16. R. T. Beyer, *Nonlinear Acoustics,* Washington, DC: Department of the Navy, Naval Sea Systems Command, 1974.
17. K. U. Ingard, *Fundamentals of Waves and Oscillations,* Cambridge, UK: Cambridge Univ. Press, 1988.
18. L. E. Kinsler et al., *Fundamentals of Acoustics,* New York: Wiley, 1982.
19. V. M. Ristic, *Principles of Acoustic Devices,* New York: Wiley, 1983.
20. D. Stansfield, *Underwater Electroacoustic Transducers,* Bath and St. Albans, UK: Bath Univ. Press and Institute of Acoustics, 1991.
21. R. F. W. Coates, *Underwater Acoustic Systems,* New York: Wiley, 1989.
22. W. M. Carey, Standard definitions for sound levels in the ocean, *IEEE J. Oceanic Eng.,* **20**: 109–113, 1995.
23. R. J. Bobber, *Underwater Electroacoustic Measurements,* Los Altos, CA: Peninsula, 1988.
24. K. G. Foote, Maintaining precision calibrations with optimal copper spheres, *J. Acoust. Soc. Am.,* **73**: 1054–1063, 1983.
25. J. A. Smith, Doppler sonar and surface waves: Range and resolution, *J. Atmos. Oceanic Technol.,* **6**: 680–696, 1989.
26. F. B. Jensen et al., *Computational Ocean Acoustics,* New York: American Institute of Physics, 1994.
27. P. H. Dahl, On the spatial coherence and angular spreading of sound forward scattered from the sea surface: Measurements and interpretive model, *J. Acoust. Soc. Am.,* **100**: 748–758, 1996.
28. J. R. Apel et al., An overview of the 1995 swarm shallow-water internal wave acoustic scattering experiment, *IEEE J. Oceanic Eng.,* **22**: 465–500, 1997.
29. S. M. Flatté et al., *Sound Transmission Through a Fluctuating Ocean,* Cambridge, UK: Cambridge Univ. Press, 1979.
30. R. E. Francois and G. R. Garrison, Sound absorption based on ocean measurements. Part i: Pure water and magnesium sulfate contributions. Part ii: Boric acid contribution and equation for total absorption, *J. Acoust. Soc. Am.,* **72**: 896–907, 1879–1890, 1982.
31. D. R. Jackson et al., Tests of models for high-frequency seafloor backscatter, *IEEE J. Oceanic Eng.,* **21**: 458–470, 1996.
32. P. D. Mourad and D. R. Jackson, High frequency sonar equation models for bottom backscatter and forward loss, *OCEANS '89 Conf. Proc.,* 1989, pp. 1168–1175.
33. K. L. Williams and D. R. Jackson, Bistatic bottom scattering: Model, experiments, and model/data comparison, *J. Acoust. Soc. Am.,* **103**: 169–181, 1998.
34. P. H. Dahl and W. L. J. Fox, Measurement and interpretation of angular spreading from multiple boundary interactions in a shallow water channel, in N. G. Pace et al. (eds.), *High Frequency Acoustics in Shallow Water,* La Spezia, Italy, 1997, pp. 107–114.
35. B. Nützel and H. Herwig, A two-frequency hydroacoustic scatterometer for bubble scattering investigations, *IEEE J. Oceanic Eng.,* **19**: 41–47, 1994.
36. H. Medwin, *In situ* acoustic measurements of microbubbles at sea, *J. Geophys. Res.,* **82**: 971–976, 1977.
37. J. Dalen and A. Løvik, The influence of wind-induced bubbles on echo integration surveys. *J. Acoust. Soc. Am.,* **69**: 1653–1659, 1981.
38. S. A. Thorpe, On the clouds of bubbles formed by breaking wind-waves in deep water, and their role in air-sea gas transfer, *Philos. Trans. R. Soc. London A,* **304**: 155–210, 1982.

39. S. Vagle and D. M. Farmer, The measurement of bubble-size distributions by acoustical backscatter, *J. Atmos. Oceanic Technol.,* **9**: 630–644, 1992.

40. M. Gensane, Bubble population measurements with a parametric array, *J. Acoust. Soc. Am.,* **95**: 3183–3190, 1994.

41. P. H. Dahl and A. T. Jessup, On bubble clouds produced by breaking waves: An event analysis of ocean acoustic measurements, *J. Geophys. Res.,* **100**: 5007–5020, 1995.

42. H. Medwin, Acoustic fluctuations due to microbubbles in the near-surface ocean, *J. Acoust. Soc. Am.,* **56**: 1100–1104, 1974.

43. D. M. Farmer and S. Vagle, Waveguide propation of ambient sound in the ocean-surface layer, *J. Acoust. Soc. Am.,* **86**: 1897–1908, 1989.

44. K. W. Commander and A. Prosperetti, Linear pressure waves in bubbly liquids: Comparison between theory and experiments, *J. Acoust. Soc. Am.,* **85**: 732–746, 1989.

45. E. Lamarre and W. K. Melville, Sound-speed measurements near the ocean surface, *J. Acoust. Soc. Am.,* **96**: 3605–3616, 1994.

46. H. C. Pumphrey and L. A. Crum, Free oscillations of near-surface bubbles as a source of the underwater noise of rain, *J. Acoust. Soc. Am.,* **87**: 142–148, 1990.

47. P. A. Crowther and A. Hansla, The lifetimes, vortices and probable origins of sonic and ultrasonic noise sources on the sea surface, in B. B. Kerman (ed.), *Natural Physical Sources of Underwater Sound,* Boston: Kluwer Academic, 1993, pp. 379–392.

48. P. H. Dahl, High frequency noise emitted from ocean breaking waves, in M. J. Buckingham and J. R. Potter (eds.), *Sea Surface Sound '94: Third International Meeting on Natural Physical Processes Related to Sea Surface Sound,* New York: World Scientific Press, 1995, pp. 174–184.

49. S. Vagle and D. M. Farmer, A comparison of four methods for bubble size and void fraction measurements, *IEEE J. Oceanic Eng.,* **23**: 211–222, 1998.

50. C. Devin, Survey of thermal, radiation, and viscous damping of pulsating air bubbles in water, *J. Acoust. Soc. Am.,* **31**: 1651–1667, 1959.

51. K. Commander and E. Moritz, Off-resonance contributions to acoustical bubble spectra, *J. Acoust. Soc. Am.,* **85**: 2665–2669, 1989.

52. P. A. Elmore et al., Effects of bubbles on high-frequency sound propagation in very shallow water, *Proc. 16th Int. Congr. Acoust. and 135th Meeting Acoust. Soc. Am.,* 1998, pp. 709–710.

53. O. A. Mathisen, Acoustic assessment of stocks of fish and krill, *Proc. 6th Conf. Comité Arct. Int.,* New York, 1989, pp. 556–581.

54. D. Gaudet, Enumeration of migratory salmon populations using fixed-location sonar counters, *Rapp. P.-V. Reun., Cons. Int. Explor. Mer.,* **189**: 197–209, 1990.

55. M. V. Trevorrow, Detection of migratory salmon in the fraser river using 100-kHz sidescan sonars, *Can J. Fish. Aquat. Sci.,* **54**: 1619–1629, 1997.

56. P. H. Dahl and O. A. Mathisen, Some experiments and considerations for development of doppler-based riverine sonars, *IEEE J. Oceanic Eng.,* **9**: 214–217, 1984.

57. D. V. Holliday and R. E. Pieper, Bioacoustical oceanography at high frequencies, *ICES J. Mar. Sci.,* **52**: 279–296, 1995.

58. A. Ishimaru, *Wave Propagation and Scattering in Random Media,* New York: Academic Press, 1978.

59. F. Masahiko, K. Ishii, and Y. Miyanohana, Attenuation of sound by schooling fish, *J. Acoust. Soc. Am.,* **92**: 987–994, 1992.

60. K. G. Foote, Importance of the swimbladder in acoustic scattering by fish: A comparison of gadoid and mackerel target strengths, *J. Acoust. Soc. Am.,* **67**: 2084–2089, 1980.

61. P. H. Dahl and O. A. Mathisen, Measurement of fish target strength and associated directivity at high frequencies, *J. Acoust. Soc. Am.,* **73**: 1205–1211, 1983.

62. D. V. Holliday and R. E. Pieper, Volume scattering strengths in zooplankton distributions at acoustic frequencies between 0.5 and 3 MHz, *J. Acoust. Soc. Am.,* **67**: 135–146, 1980.

63. T. K. Stanton, C. S. Clay, and D. Chu, Ray representation of sound scattering by weakly scattering deformed fluid cylinders: Simple physics and application to zooplankton, *J. Acoust. Soc. Am.,* **94**: 3454–3462, 1993.

64. T. K. Stanton et al., Average echoes from randomly oriented random-length finite cylinders: Zooplankton models, *J. Acoust. Soc. Am.,* **94**: 3463–3472, 1993.

65. R. Pinkel, Observations of strongly nonlinear internal motion in the open sea using a range-gated doppler sonar, *J. Phys. Ocean.,* **9**: 675–686, 1979.

66. R. Pinkel, On the use of doppler sonar for internal wave measurements, *Deep-Sea Res.,* **28**: 269–289, 1981.

67. A. J. Plueddemann and R. Pinkel, Characterization of the patterns of diel migration using a Doppler sonar, *Deep-Sea Res.,* **36**: 509–530, 1989.

68. L. Goodman, Acoustic scattering from ocean microstructure, *J. Geophys. Res.,* **95**: 11557–11573, 1990.

69. L. Goodman and K. A. Kemp, Scattering from volume variability, *J. Geophys. Res.,* **86**: 4083–4088, 1981.

70. H. E. Seim, M. C. Gregg, and R. T. Miyamoto, Acoustic backscatter from turbulent microstructure, *J. Atmos. Oceanic Technol.,* **12**: 367–372, 1995.

71. T. K. Stanton et al., Acoustic characterization and discrimination of marine zooplankton and turbulence, *ICES J. Mar. Sci.,* **51**: 469–479, 1994.

72. R. D. M. Nash et al., Distribution of peaks of 70 kHz acoustic scattering in relation to depth and temperature during day and night at the edge of the gulf stream—echofront 83, *Deep-Sea Res.,* **36**: 587–596, 1990.

73. O. A. Mathisen and M. C. Macaulay, The morphological features of a super swarm of krill, *Euphausia superba, Mem. Natl. Inst. Polar Res. Spec. Issue (Jpn.),* (27), 153–164, 1983.

74. R. Pinkel et al., Solitary waves in the western equatorial Pacific Ocean, *Geophys. Res. Lett.,* **24**: 1603–1606, 1997.

75. D. R. Jackson et al., High-frequency bottom backscatter measurements in shallow water, *J. Acoust. Soc. Am.,* **80**: 1188–1199, 1986.

76. P. H. Dahl et al., Simultaneous acoustic and microwave backscattering from the sea surface, *J. Acoust. Soc. Am.,* **101**: 2583–2595, 1997.

77. S. T. McDaniel, Sea surface reverberation: A review, *J. Acoust. Soc. Am.,* **94**: 1905–1922, 1993.

78. P. H. Dahl and W. J. Plant, The variability of high-frequency acoustic backscatter from the region near the sea surface, *J. Acoust. Soc. Am.,* **101**: 2596–2602, 1997.

79. H. Matsumoto, R. Dziak, and C. G. Fox, Estimation of seafloor microtopographic roughness through modeling of acoustic backscatter data recorded by multibeam sonar systems, *J. Acoust. Soc. Am.,* **94**: 2777–2787, 1993.

80. D. R. Jackson, K. L. Williams, and K. B. Briggs, High-frequency acoustic observations of benthic spatial and temporal variability, *Geo-Marine Lett.,* **16**: 212–218, 1996.

81. P. H. Dahl, Bistatic sea surface scattering: A model and its comparison with integral field measurements, *J. Acoust. Soc. Am.,* In press, 1999.

82. J. S. Jaffe et al., FTV: a sonar for tracking macrozooplankton in three dimensions. *Deep-Sea Res. I,* **42**: 1495–1512, 1995.

83. E. O. Belcher and D. C. Lynn, An application of tapered, PZT composite lenses in an acoustic imaging sonar with 1-cm resolution, *OCEANS '97 MTS/IEEE Conf. Proc.,* 1997, pp. 1043–1047.

84. E. O. Belcher, Application of thin, acoustic lenses in a 32-beam, dual-frequency, diver-held sonar, *OCEANS '96 MTS/IEEE Conf. Proc.,* 1996, pp. 767–772.

85. E. O. Belcher, Thin, acoustic lenses applied in a 64-beam, 75-kHz diver-held sonar, *OCEANS '97 MTS/IEEE Conf.Proc.,* 1997, pp. 451–456.

PETER H. DAHL
Applied Physics Laboratory
College of Ocean and Fishery Sciences
University of Washington